Decorated Tetrathiafulvalene-Based Ligands: Powerful Chemical Tools for the Design of Single-Molecule Magnets

Olivier Cador, Boris Le Guennic, Lahcène Ouahab, Fabrice Pointillart

Decorated Tetrathiafulvalene-Based Ligands: Powerful Chemical Tools for the Design of Single-Molecule Magnets

Olivier Cador,[a] Boris Le Guennic,[a] Lahcène Ouahab,[a] Fabrice Pointillart,*[a]

Abstract: This Minireview covers the design and characterization of coordination lanthanide complexes involving TTF-based ligands. The specific design of TTF-based ligands allowed the isolation of complexes with magnetic properties such as Single-Molecule Magnets (SMMs) behavior and the studies of magnetic modulations due to supramolecular interaction, molecular engineering, magnetic dilution as well as isotopic enrichment. A careful design lead to TTF-based ligands displaying several coordination sites in order to rationally elaborate polynuclear systems with multi-SMM behavior or to auto-assembly SMMs. Their redox-activity allowed the investigation of coordination lanthanide complexes in several oxidation states and their consequences on optical and magnetic properties. The complete experimental and theoretical studies of such systems contributed to the understanding of the magnetic properties of lanthanide ions for futures applications in high density storage and quantum computing.

Introduction

The 2,2'-bis(1,3-dithiolylidene) organosulfur molecule (tetrathiafulvalene, TTF) was discovered in the early 70s[1] and was used first to design conducting materials such as organic metals, semiconductors and superconductors.[2-5] The TTF core can be easily decorated replacing the hydrogen atoms by one to four substituents able to bring new properties, for example, to develop photo-functional materials[6-8] or able to coordinate paramagnetic transition metals.[9] A plethora of different coordinating groups was used over the years such as amino, nitrilo, phenolate, phosphino, β-diketonate, pyrazine, pyrimidine, pyridine, pyridine-N-oxide, bipyridine groups.[10] In the early 2000s, first attempts of coordination with lanthanide ions appeared[11] and few years later the first X-ray structure of a lanthanide coordination complex involving a TTF-based ligand was published.[12] The objective of the lanthanide insertion in the TTF-based coordination complex was to take advantage of their intrinsic emission and specific magnetic properties. The luminescence of the lanthanide ranges from the visible to the near-infrared (NIR) energy and it is characterized by line-sharp emission bands. Thus lanthanide materials are at the origin of applications in OLEDs, bio- and microscopy imaging, sensors or time-resolved luminescent immunoassays[13-17] but due to the forbidden f-f transitions,[18] the use of organic chromophores is needed to increase the efficiency of the sensitization process of such ions through antenna effect.[19-22] In particular case of the use of push-pull organic chromophore in the sensitization process, TTF-based ligands are very efficient.[23-25] However this review is mainly focuses on the magnetic properties which could be obtained for TTF-based coordination lanthanide complexes especially the observation of Single-Molecule Magnet (SMM) behavior. Such phenomena might have potential applications in high density data storage, quantum computing and spintronics.[26-31] The interest for lanthanides in the elaboration of SMMs grown up in the 2000s after the discovery of the first mononuclear lanthanide SMM.[32] Recently few groups have shown that lanthanide SMM could displayed a blocking temperature close[33-35] or even above[36] the liquid nitrogen temperature using an organometallic approach. The advantages to use TTF-based ligand in the design of lanthanide SMMs are i) the possibility to get high resolution emission, ii) the redox-activity of the TTF ligand and iii) to open the route to the design of redox switching SMMs.

Few years ago, some of us published a review focused on both the magnetic and optical properties of TTF-based lanthanide SMMs and their correlation.[37] In the present review, we wished to show how using the common TTF-based molecular skeleton 2-(4,5-bis(propylthio)tetrathiafulvalenyl)-1H-benzimidazol-2-yl)-pyridine (**L^1**) (Scheme 1), it was possible to design a library of TTF-based ligands by alkylation of **L^1**. Thus 4,5-bis(propylthio)-tetrathiafulvalene-2-(2-pyridyl)-benzimidazole methyl-2-pyridine (**L^2**), 2-{1-[methylbenzo(1-oxyl-3-oxide-4,4,5,5-tetramethylimidazoline)]-4,5-[4,5-bis(propylthio)-tetrathiafulvalenyl]-1H-benzimidazol-2-yl}pyridine (**L^3**), 2-{1-[4,4'-dimethyl-2,2'-bipyridyl]-4,5-[4,5-bis(propylthio)-tetrathiafulvalenyl]-1H-benzimidazol-2-yl}pyridine (**L^4**), 2-(1-(2,6-di(pyrazol-1-yl)-4-methylpyridyl)-4,5-(4,5-bis(propylthio)-tetrathiafulvalenyl)-1H-benzimidazol-2-yl)-pyridine (**L^5**) and 2-(1-(4'-[4-(methylphenyl)]-2,2:6',2"-terpyridyl)-4,5-(4,5-bis(propylthio)-tetrathiafulvalenyl)-1H-benzimidazol-2-yl)-pyridine (**L^6**), 2-{1-methylpyridine-N-oxide-4,5-[4,5-bis(propylthio)tetrathiafulvalenyl]-1H-benzimidazol-2-yl}pyridine ligand (**L^7**) and 2-{1-[2-methyl[6]helicene]-4,5-[4,5-bis(propylthio)tetrathiafulvalenyl]-1H-benzimidazol-2-yl}pyridine (**L^8**) (Scheme 1) were elaborated. So now in addition to what we reported in our previous review,[37] the elaboration of a complete library of ligands allows the rational design of both mononuclear and polynuclear complexes opening new investigations such as i) the enhancement of the magnetic properties by isotopic enrichment, ii) the introduction of a paramagnetic specie, iii) the design of multi-SMM systems, iv) the auto-assembly of SMMs and v) the introduction of chiral elements.

[a] O.C. B.L.G. L.O. F.P.
Univ Rennes, CNRS, ISCR (Institut des Sciences Chimiques de Rennes) - UMR 6226, F-35000 Rennes, France.
fabrice.pointillart@univ-rennes1.fr

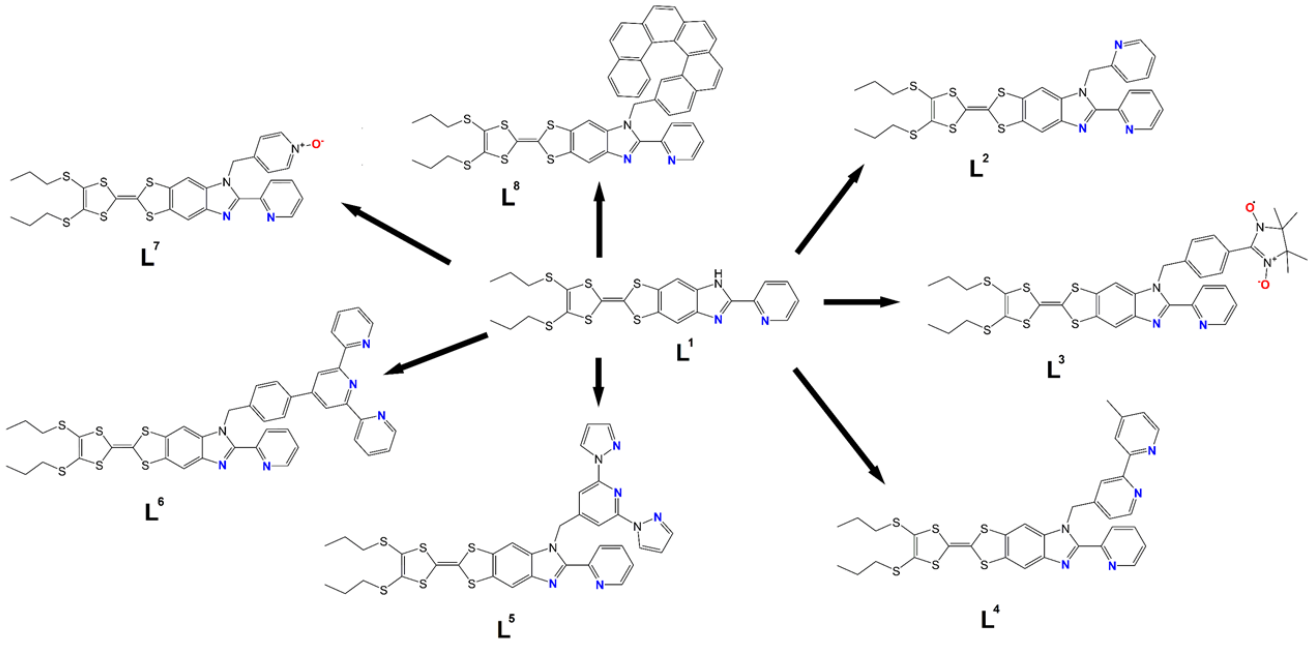

Scheme 1. Molecular structures of the ligands $\mathbf{L^1}$-$\mathbf{L^8}$.

Supramolecular Effect on the Single-Molecule Magnet Behavior

Hydrogen Bond Effect

The molecular skeleton $\mathbf{L^1}$ which is a common chemical fragment to all the ligand $\mathbf{L^2}$-$\mathbf{L^8}$ can be used as a ligand for the coordination of various metal centers through its bischelating benzimidazole-2-pyridine (bzip) moiety (Scheme 1). $\mathbf{L^1}$ was obtained by the direct condensation reaction between the commercial 2-pyridinecarboxaldehyde and the 5,6-diamino-2-[4,5-bis(propylthio)-1,3-dithio-2-ylidene]benzo[d]-1,3-dithiole.[38,39] The association of $\mathbf{L^1}$ with the $Dy(hfac)_3{\cdot}2H_2O$ Lewis acid precursor led to the mononuclear complex of formula $[Dy(hfac)_3(\mathbf{L^1})]$ (**1**) (with $hfac^-$ = 1,1,1,5,5,5-hexafluoroacethylacetonate) in which the Dy(III) center is linked to a C_{2v} N2O6 coordination environment.[40] The crystal packing highlighted the formation of dimers through hydrogen bonds between the amine and an $hfac^-$ anion (Figure 1). Dynamic magnetic measurements of **1** did not show any SMM behavior in solid state. Once in frozen CH_2Cl_2 solution, **1** presented an out-of-phase contribution of its magnetic susceptibility which is an indication of slow magnetic relaxation. The temperature dependence of the relaxation time followed the combination of a thermally activated regime (Orbach process) at high temperature with Δ = 12(1) K, $\tau_0 = 1.9(4)\times10^{-6}$ s and a thermally independent regime (QTM process) at low temperature with $\tau_{TI} = 2.14(8)\times10^{-5}$ s. The small determined energy barrier is a strong indication of the involvement of a Raman process in the magnetic relaxation mechanism as demonstrated recently for a Dy(III) ion in a similar coordination environment (see the "Chiral Single-Molecule Magnet" section of this review).

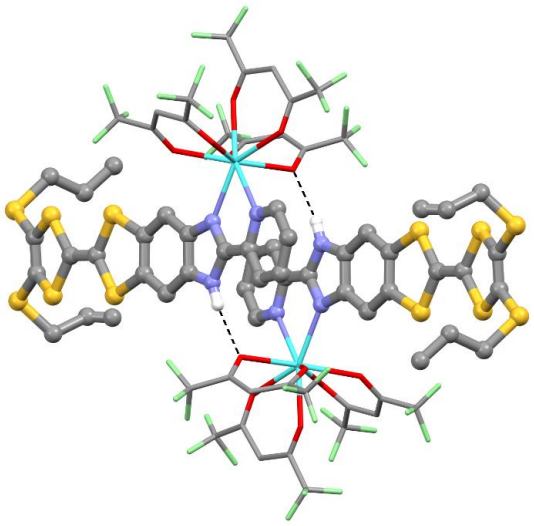

Figure 1. Representation of two neighboring complexes of $[Dy(hfac)_3(\mathbf{L^1})]$ (**1**) forming a dimer through hydrogen bonds. Ligand $\mathbf{L^1}$ is represented in ball and sticks while the $Dy(hfac)_3$ fragment is represented in capped sticks. Color code: carbon: grey, nitrogen: blue, oxygen: red, Sulfur: yellow, fluoride: light green, hydrogen: white and dysprosium: light blue. Adapted from ref [39].

Assuming that hydrogen bonds are broken in dichloromethane solution, the first hypothesis was to attribute the non-observation of the slow magnetic relaxation to the presence of hydrogen bonds. In order to verify such hypothesis, $\mathbf{L^1}$ was

chemically modified to cancel the hydrogen bond network by alkylating the amine with the methyl-2-pyridine arm to form the ligand 4,5-bis(propylthio)-tetrathiafulvalene-2-(2-pyridyl)-benzimidazole methyl-2-pyridine (**L²**) (Scheme 1).[40] Once associated with the $Dy(hfac)_3{\cdot}2H_2O$ precursor, a similar mononuclear complex of formula $[Dy(hfac)_3(\mathbf{L^2})]$ was formed (Figure 2). In absence of dimerization through hydrogen bonds, **2** behaved as a SMM in both solid- (Δ = 17.2(9) K, $\tau_0 = 9.5(2)\times10^{-6}$ s and $\tau_{TI} = 1.71(2)\times10^{-4}$ s) and solution-state (Δ = 15(2) K, $\tau_0 = 1.5(3)\times10^{-6}$ s and $\tau_{TI} = 2.69(8)\times10^{-5}$ s). In other words, both compounds **1** and **2** behaved similarly at the molecular level (in frozen solution) while they presented drastically different magnetic behavior when the supramolecular organization plays a role (solid-state).

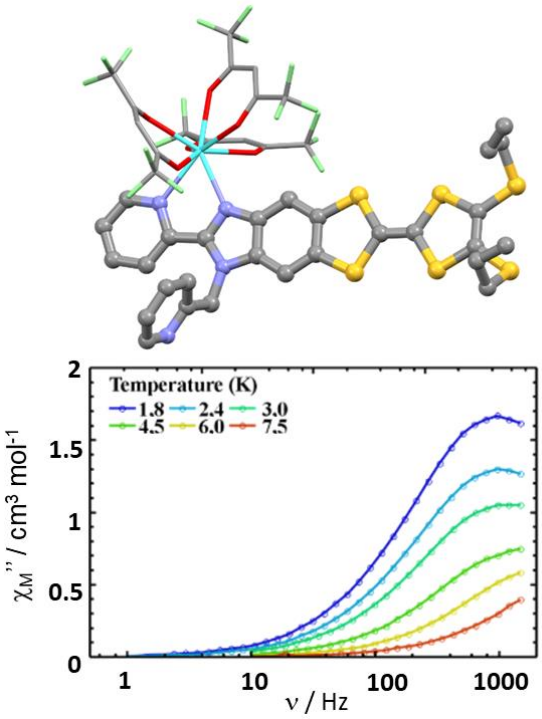

Figure 2. (Top) X-ray structure of $[Dy(hfac)_3(\mathbf{L^2})]$ (**2**) and (bottom) the frequency dependence of its out-of-phase signal χ_M" measured in solid-state between 1.8 and 7.5 K at H = 0 Oe. Ligand **L²** is represented in ball and sticks and the $Dy(hfac)_3$ fragment is represented in capped sticks. Color code: carbon: grey, nitrogen: blue, oxygen: red, Sulfur: yellow, fluoride: light green, hydrogen: white and dysprosium: light blue. Adapted from ref [39].

The role of hydrogen bonds in the magnetic switching of the SMM behavior was confirmed and rationalized in 2014 by ab initio calculations.[41] In the objective to have a maximum of experimental data to compare with the theoretical ones and thank to the fact that **1** crystallizes in the P-1 space group, single-crystal angular-resolved magnetometry measurements were performed (Figure 3a). Such experiment permitted to determine the components of the g-factor (g_z = 14.22, g_y = 3.96 and g_x = 9.43) which are far from an Ising-type anisotropy (g_z = 20, g_y = 0 and g_x = 0) but in agreement with the non-observation of a SMM behavior in solid-state for **1**. Ab initio calculations performed for an isolated molecule of **1** (no hydrogen bond) led to an almost Ising-type anisotropy ground state (g_z = 18.87, g_y = 0.16 and g_x = 0.08) composed by 85% of $M_J = \pm 15/2$ and an energy gap with the first excited state of 91.1 cm^{-1}. Such results demonstrated the necessity to take into account the supramolecular organization through the hydrogen bond to reproduce the experimental magnetic data.

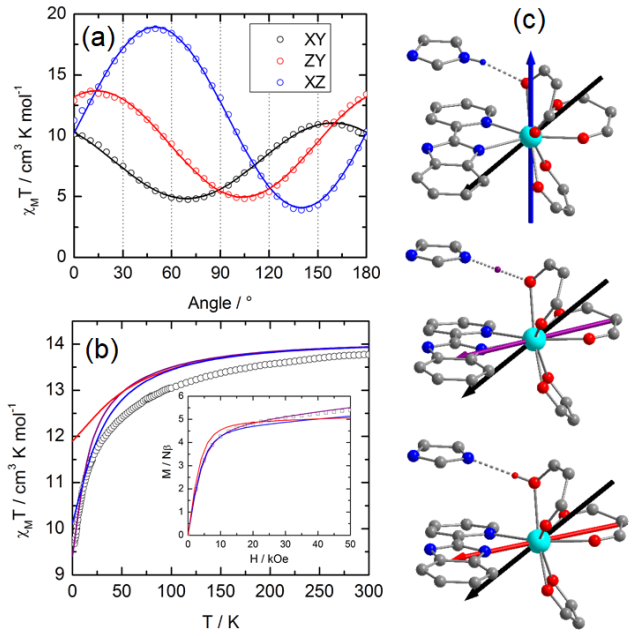

Figure 3. (a) Angular dependence of the $\chi_M T$ product for **1** in the three orthogonal planes (open circles). The full lines represent the best fitted curves. (b) Thermal dependence of the magnetic susceptibility for **1** with the curves calculated on the basis of SA-CASSCF/RASSI-SO data for different positions of the hydrogen atom involved in the hydrogen bond (H_N, blue line; H_m, purple line and H_O, red line) (c) Orientation of the experimental ground-state anisotropy axes (black arrow) and calculated ground-state anisotropy axis in function of the positions of the hydrogen atom (H_N, blue arrow; H_m, purple arrow and H_O, red arrow). Color code: carbon: grey, nitrogen: blue, oxygen: red and dysprosium: light blue. Adapted from ref [40].

Three various arbitrary positions of the hydrogen atom were considered: i) close to the oxygen atom of the $hfac^-$ anion with a classical O-H distance (H_O), ii) at the position calculated by X-ray diffraction on single crystal (H_N) and iii) equidistant to the nitrogen and oxygen atoms (H_m) (Figure 3c). While the H_O position led to an Ising-type anisotropy (g_z = 19.51, g_y = 0.03 and g_x = 0.02) composed by 94% of $M_J = \pm 15/2$ and an energy gap with the first excited state of 109.7 cm^{-1} the H_N position led to a mixing of M_J Kramers doublets as ground state but with a strong discrepancy of orientation between the experimental and calculated anisotropy of the ground state (67°). A satisfactory agreement between calculations and experiment was found for the hydrogen atom localized at equidistance to the nitrogen and oxygen atoms. The g-factor highlighted significant transversal components (g_z = 17.05, g_y = 3.05 and g_x = 0.83) explaining the fast magnetic relaxation in the solid-state while the ground state reproduced the

experimental magnetization and the calculated splitting reproduced the thermal variation of the magnetic susceptibility (Figure 3b). The position of the hydrogen atom involved in the hydrogen bond influences the charge carried out by the oxygen atom of the $hfac^-$ anion and thus modified the electronic distribution around the Dy(III) ion and finally induced drastic modulation of the magnetic response.

Magneto-structural correlation

In the previous section, it was demonstrated the important role of ab initio calculations to rationalize unconventional magnetic behaviors. The magnetism of lanthanide-based systems is driven by the energy splitting of the ground state which is also at the origin of the sharp emission bands of the lanthanide since they are assigned to transitions from the emitting state to the various J levels of the ground state. The latter is further split into M_J states due to the crystal field effect that can be detected by well-resolved emission spectroscopy. In other words both lanthanide luminescence and magnetism have the same origin and lanthanide luminescence could be seen as a photography of the energy splitting and could be an experimental probe to endorse the magnetic and computational results.[37],[42-55] Since the Dy(III) emission of complexes **1** and **2** was not observable because of the strong absorption of the ligands $\mathbf{L^1}$ and $\mathbf{L^2}$ in the whole visible range, the Yb(III) analogues [Yb(hfac)$_3$($\mathbf{L^1}$)] (**3**) and [Yb(hfac)$_3$($\mathbf{L^2}$)] (**4**) were synthetized.[56] The thermal dependence of the magnetic susceptibility for both Yb(III) analogues were first fitted evaluating the crystal field by the Stevens method. This equivalent operator model was expressed as polynomials of the total angular momentum matrices (J^2, J_z, J_+ and J_-) in $\boldsymbol{O_k^q}$ operators.[57-59]

$$H = \sum_{k=2,4,6} \sum_{q=-k}^{k} B_k^q \boldsymbol{O_k^q}$$

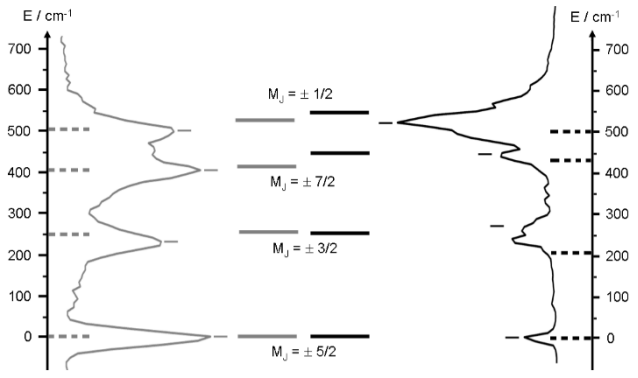

Figure 4. The full grey (compound **3**) and black (compound **4**) lines correspond to the solid-state emission spectra at 77 K represented with an appropriate shift of the energy scale in the $^2F_{5/2} \rightarrow {}^2F_{7/2}$ NIR region. The full horizontal sticks illustrated the energy splitting determined by Stevens' method from the magnetic data while the dashed horizontal sticks illustrated the energy splitting obtained by MS-CASPT2/RASSI-SO calculations. Adapted from ref [56].

To prevent the over parametrization, the highest symmetry as possible was considered *i.e.* D_{2d} for **3** and D_{4d} for **4**. Thus the eigenstates are found pure for **4** while the M_J states are mixed for **3**. The following 0, 259, 416, 522 cm^{-1} and 0, 251, 459, 544 cm^{-1} experimental energy splittings were found for **3** and **4**, respectively. In parallel, the calculated energy splitting was found for the two compounds at the CASSCF/MS-PT2/RASSI-SO level. The same procedure than the one used for the Dy(III) analogues was employed giving g_z = 5.8 and g_z = 5.3 (expected value 5.71 for a pure M_J = 5/2 ground state) and energy spittings of 0, 252, 407, 504 cm^{-1} and 0, 210, 436, 503 cm^{-1} for **3** and **4** respectively, offering great correlation with luminescence results (Figure 4). The high resolved emission was guaranteed by a sensitization mechanism of the Yb(III) emission which involved a photo-induced electron transfer (PET).[11,60-65] The near infrared luminescence for **3** and **4** are composed of four main contributions as expected for an $^2F_{7/2}$ ground state leading to the experimental energy splittings of 0, 234, 409, 504 cm^{-1} and 0, 284, 448, 533 cm^{-1} respectively for **3** and **4**.

Enhancement of the Single-Molecule Magnet Performances

Simple mononuclear complexes were designed and their magnetic properties were interpreted thanks to the help of ab initio calculations. The objective of this section is now to show how the performances of the SMM can be enhanced. To do so, three strategies were proposed: i) a modulation of the electronic distribution by molecular engineering, [66] ii) magnetic dilution[67] and iii) isotopic enrichment.[68-76]

Molecular Engineering: electronic distribution

Compound **2** displayed SMM behavior in both solid-state and frozen solution but its performances remained modest with a maximum of the χ_M" data localized at 1000 Hz at 2 K (Figure 2). It is well known that the series of lanthanide ions can be divided in two families depending of their electronic distribution shape i.e. the oblate ions for those with 4f electrons mainly localized in a plane and the prolate ions for those with 4f electrons mainly localized along an axis. Thus, in first approximation, to optimize the spin-orbit coupling, the electronic repulsion between the 4f electrons and the electrons coming from the ligands must be minimized. Consequently, the molecular design is able to drive the electronic distribution around the metal centre. In the literature different strategies have been used and proved their worth: playing with the steric hindrance[33-36] and electron withdrawing/donating substituents,[66,77] adding axial or equatorial ligands.[78,79] In the context of this review, the charge density in the first coordination sphere of the Dy(III) ion in **2** was reorganized by replacing the $hfac^-$ anions with tta^- anions (tta^- = 2-thenoyltrifluoroacetonate). Indeed, the negative charges on the oxygen atoms of the diketonate ligands increased in the tta^- anions because the thiophene moiety is less electro-attractive than the CF_3 one. The resulting mononuclear complex [Dy(tta)$_3$($\mathbf{L^2}$)]·C_6H_{14} (**5**) has a very similar structure than **2** (Figure

5).[80] **5** displayed a SMM behavior in zero applied magnetic field with a maximum of the out-of-phase component of the magnetic susceptibility at 2 K which is centred at 65 Hz (Figure 5). At such temperature, **5** presented a magnetic relaxation 15 times slower than **2**. The experimental orientation of the anisotropy axis was experimentally determined perpendicular to the plane formed by the Dy(III) ion and the two nitrogen atoms of the imidazole-pyridine rings in agreement with the oblate character of the Dy(III) ion. CASSCF/RASSI-SO calculations allowed to determine the nature of the ground state easy axis ($M_J = \pm 15/2$, $g_z = 19.50$) which is almost parallel to the experimental one (deviation of 7.6°). The thermal dependence of the relaxation time was determined thank to an extended Debye model[81] and it was fitted by a combination of thermal dependent Orbach and QTM ($\tau_{TI} = 1.62(4) \times 10^{-3}$ s) regimes. The extracted energy barrier for **5** (Δ = 40 K) is twice the value found for **2** (Δ = 18 K). The experimental energy barrier value is smaller than the calculated energy gap between the ground and the first excited states (194 K). Such discrepancy was recently explained by the significant contribution of the Raman process in such systems.[82-84]

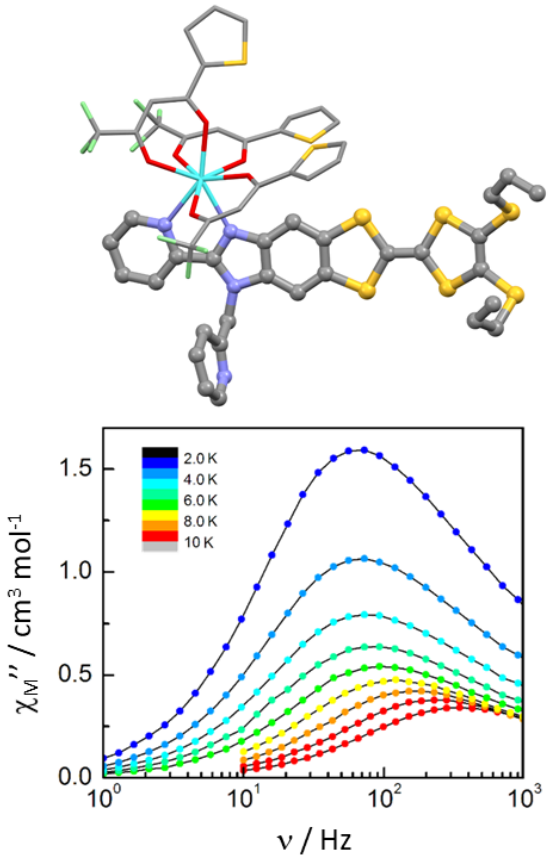

Figure 5. (top) Molecular structure of $[Dy(tta)_3(\mathbf{L^2})]\cdot C_6H_{14}$ (**5**). Ligand $\mathbf{L^1}$ is represented in ball and sticks and the $Dy(tta)_3$ fragment is represented in capped sticks. Color code: carbon: grey, nitrogen: blue, oxygen: red, sulfur: yellow, fluoride: light green and dysprosium: light blue. (bottom) Frequency dependence of the out-of-phase component χ_M" of the magnetic susceptibility in the temperature range 2-10 K at 0 Oe. Adapted from ref [80].

The substitution of the $hfac^-$ with tta^- led to a relaxation of the magnetization slow enough to permit the observation of a butterfly shaped hysteresis loop until 4 K with a maximum coercive field of 700 Oe. The presence of the TTF moiety allowed an easy check of the stability of the complex in CH_2Cl_2 solution by the red shift (2100 cm^{-1}) of the Intra-Ligand Charge Transfer (ILCT) excitation after complexation. Thus the hysteresis loop remained in frozen CH_2Cl_2 solution and can be recorded by irradiation of the ILCT band by Magnetic Circular Dichroism (MCD) measurements.[85-87] The Yb(III) analogue was also synthetized in order to perform structural correlation between magnetism and luminescence as previously detailed in this review for the compounds **3** and **4**.[88]

Dipolar Interactions: Magnetic Dilutions

The limitation of the SMM performances comes mainly from the fast relaxation of the magnetization through QTM that is operating via the mixing of $+M_J$ and $-M_J$ states. For Kramers ions (half-integer Spin) these states are degenerate and QTM is not theoretically allowed. Nevertheless, this degeneration is released in presence of an applied magnetic field, hyperfine coupling and dipolar interactions. The latter interactions are present in the condensed phase when the molecules are close enough to generate an internal field. Such internal field can be cancelled by magnetic dilution i.e. doping a diamagnetic matrix with the SMM. This matrix can be a solvent[39] or a diamagnetic analogue of the SMM.[67,89] When the dynamical magnetic properties of a frozen solution (C = 7.7 mM) of **5** ($\mathbf{5_{solution}}$) is measured, the SMM behavior is retained and the maximum of the out-of-phase component of the magnetic susceptibility at 2 K shift from 65 Hz for the condensed phase to 10 Hz for the solution.

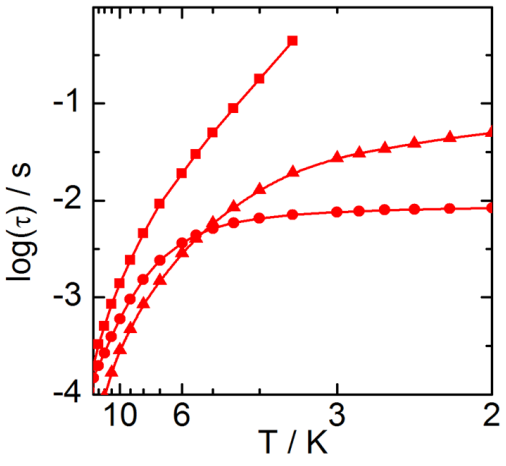

Figure 6. Thermal dependence of the relaxation time for a given isotope of bulk sample **5** in solid-state (full red disks), frozen CH_2Cl_2 solution (full red triangles) and diluted $[Y_{0.96}{}^{164}Dy_{0.04}(tta)_3(\mathbf{L^2})]$ (full red squares). Adapted from ref [90].

Taking into account the concentration, one can deduce that the average distance between the Dy(III) centres is about 60 Å in the frozen solution versus 10 Å in the condensed phase

explaining the slower magnetic relaxation at low temperature (Figure 6). Even more efficient to slow down the magnetic relaxation is the magnetic dilution in the solid-state doping the diamagnetic Y(III) analogue with 4 % of **5**. The diluted sample $[Y_{0.96}{}^{164}Dy_{0.04}(tta)_3(\mathbf{L^2})]$ (**^{164}5@Y**) presented a magnetic relaxation 10 time slower than the condensed analogue at 3.5 K (Figure 6). In conclusion the following trend was observed $\tau(\mathbf{5}) < \tau(\mathbf{5_{solution}}) < \tau(\mathbf{^{164}5@Y})$.

Hyperfine Interactions: Isotopic Enrichments

In the previous section, the SMM performances were enhanced removing the dipolar interaction. . Up to now, the best SMMs are obtained through organometallic approaches because the QTM is reduced by the strong axiality of the crystal field of the Dy(III) ion[33-36] and the magnetic dilution could be applied to enhance their magnetic performances. Nevertheless and as already said in this review, the degeneracy of the ground state cannot be removed in absence of magnetic field because of the Kramer's theorem, but, the combination of different Stevens operators acting in low symmetry can lead to the mixing of the $|J_z = \pm 15/2>$ and $|J_z = \pm 13/2>$ components.[91] Then these two components can be mixed through the transverse part because of the coupling between electrons and nucleus giving rise to a quantum tunneling of the magnetization.[92,93] In other words, the performances of the SMM could be enhanced removing the hyperfine coupling ($H_{hf} = A_{hf}IJ$ where A_{hf} is the coupling constant, I and J are the nuclear spin and electronic angular moment). Consequently a complementary strategy to the control of the crystal field by chemical design consists in the substitution of the natural isotope of the metal center with a pure metal isotope with a nuclear spin ($I \neq 0$) and without nuclear spin ($I = 0$).[68-70] In the case of Dysprosium, the natural element is mainly composed of four stable isotopes i.e. ^{161}Dy (I = 5/2, 18.9%), ^{162}Dy (I = 0, 25.5%), ^{163}Dy (I = 5/2, 24.9%) and ^{164}Dy (I = 0, 28.2%).[94] In 2015, the isotopic enrichment of **5** with both ^{161}Dy (**^{161}5**) and ^{164}Dy (**^{164}5**) was realized.[90] The frequency dependence of χ_M" clearly showed that **^{164}5** relaxed slower (ν_{max} = 20 Hz at 2 K) than **^{161}5** (ν_{max} = 100 Hz at 2 K). Relaxation times for both isotopologues were extracted and their temperature dependences follow a modified Arrhenius law (Figure 7a). While the thermally dependent regime (Orbach) is not affected by the isotopic enrichment, the thermally independent regime (QTM) is strongly modified since **^{164}5** relaxed much slower (full red circles) than **^{161}5** (full blue circles) because of the difference of nuclear spin values. In other words, the difference of relaxation times between the two isotopologues is the direct observation of the metal-centered hyperfine coupling. In a second step, the isotopic enrichment was combined with the magnetic dilution to suppress the effect of the dipolar interaction which could (partially) cancel the isotopic effect and to enhance the SMM performances. Thus **^{164}5** and **^{161}5** were dispersed in an isomorphous diamagnetic matrix of Y(III) leading to the diluted samples $[Y_{0.97}{}^{161}Dy_{0.03}(tta)_3(\mathbf{L^2})]$ (**^{161}5@Y**) and $[Y_{0.96}{}^{164}Dy_{0.04}(tta)_3(\mathbf{L^2})]$ (**^{164}5@Y**). These two diluted samples relaxed slower than their condensed analogues due to the suppression of the dipolar interaction as already observed for the natural element. **^{161}5@Y** relaxed faster than **^{164}5@Y** as observed for the condensed samples.

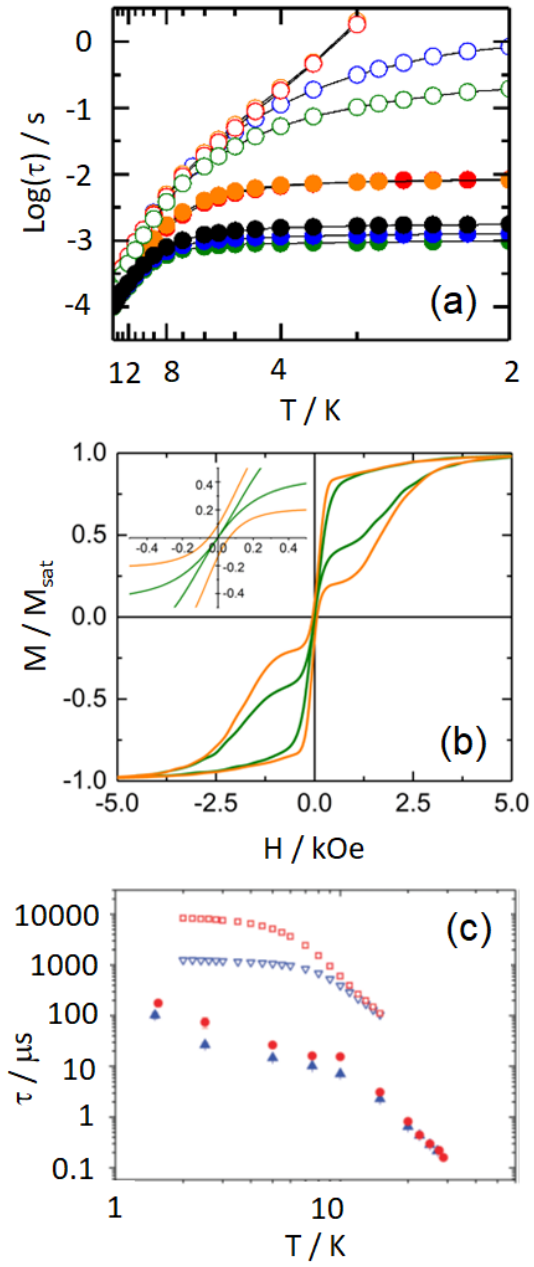

Figure 7. (a) Thermal variation of the magnetic relaxation time τ of the four isotopologues **$^{161\text{-}164}$5** (green) (full circles) and diluted samples **$^{161\text{-}164}$5@Y** (open circles) in a zero magnetic field from 2 to 15 K with blue, orange, green and red colors are attributed to the 161, 162, 163 and 164 isotopes respectively. Full lines are guides to the eye only. (b) Normalized magnetic hysteresis loops at 0.48 K and at a sweep rate of 16 Oe s^{-1} for **^{162}5@Y** (orange line) and **^{163}5@Y** (green line). The inset is a zoomed view of the origin. (c) Correlation time extracted from muon spectroscopy (full symbols) and relaxation time of magnetization obtained from ac susceptibility (empty symbols) as a function of temperature for **^{161}5** (blue) and **^{164}5** (red). Data are reported on a log-scale. Adapted from refs [96,99].

But now the difference of relaxation time of the magnetization at 2 K between **^{161}5@Y** (open blue circles) and **^{164}5@Y** (open red circles) is greater because in absence of dipolar interaction, the isotopic enrichment effect could be fully observed. Applying an external magnetic field for **^{164}5@Y** did not change the thermal dependence of the relaxation time leading to the conclusion than combining both isotopic enrichment and magnetic dilution suppressed the QTM for **^{164}5@Y**. In a third step, the two other stable isotopes (^{162}Dy and ^{163}Dy) were studied. As expected **^{162}5** (orange circles) and **^{162}5@Y** (open orange circles) (Figure 7a) behaved like their analogues involving the **^{164}Dy** isotope because I = 0 for these two isotopes. The magnetic-dipole (A) and electric-quadrupole (B) hyperfine coupling were determined equal to A = 0.0054 cm^{-1} and 0.0039 cm^{-1}, and B = 0.0385 cm^{-1} and 0.0364 cm^{-1} for ^{163}Dy and ^{161}Dy respectively.[95] Thus one could notice that the hyperfine coupling constants for the two ^{161}Dy and ^{163}Dy are not equal even if the nuclear spin is identical (I = 5/2) for both isotopes. Consequently QTM should be affected by this difference of hyperfine coupling constants. This is exactly what it was observed for the condensed **^{163}5** (full green circles) and **^{161}5** (full blue circles) (Figure 7a).[96] The effect of the hyperfine coupling constants was even better highlighted once the dipolar interaction were removed for **^{163}5@Y** (open green circles) and **^{161}5@Y** (open blue circles) (Figure 7a). The consequences of the different relaxation time of the magnetization between the spin-free and I = 5/2 isotopes could be observed measuring the hysteresis loop at 0.5 K (Figure 7b). As an example, hysteresis loops for **^{162}5@Y** (orange line) and **^{163}5@Y** (green line) are depicted on Figure 7b. Both displayed classical butterfly shaped hysteresis loop for mononuclear Dy(III) SMM[97-98] but **^{162}5@Y** highlighted remnant magnetization while **^{163}5@Y** did not (inset of Figure 7b). This study gave a clear indication that it is possible to drive the QTM through the hyperfine coupling for Ln(III) based mononuclear SMMs[70,73] since it was possible to isolate an unique chemical object displaying memory effect or not. Such result is of great interest since QTM is an obstacle for the development of high density data storage applications but is a fundamental parameter in Quantum Information Processing field (Qudits).[72]

The isotopic effect was also recently probed by Muon Spin Spectroscopy (μSR) with an increase of a factor 2 between the magnetic relaxation time of **^{161}5** and **^{164}5** in the low temperature range (QTM regime) (Figure 7c).[99] The discrepancies on the magnetic relaxation times and isotopic effect magnitude between μSR and magnetometry were explained by the local probe character of the former spectroscopy which makes it sensible to all types of fluctuation which affect the life time of the spin states. This last remark focuses the interest of such technique to study molecular spin systems as quantum gates for quantum information.[100-102]

Isotopic enrichment started then to be performed to more complex systems such as dinuclear compounds. The isotopic enrichment of the $[Dy(hfac)_3(PyNO)]_2$ (PyNO = pyridine-N-oxide)[74] in nuclear spin free and I = 5/2 Dysprosium isotopes led to almost no significant change in the magnetic behavior while for the $[(Dy(tmhd)_3)_2(bpym)]$ (tmd = tris(tetramethylheptanedionate and bpym = bipyrimidine) significant changes in the magnetic behavior were observed.[76] The difference of isotopic enrichment effect between the two systems might be attributed to the difference of intramolecular magnetic interaction magnitude and/or the difference of spin-phonon coupling and thus modulating the direct relaxation process.

Oxidation states of a tetrathiafulvalene-based Single-Molecule Magnet

The high popularity of the tetrathiafulvalene-based ligands comes from their ability to behave as reversible, strong electron-donating species. Thus one way to reach multifunctional materials is to combine the electronic conductivity with other physical properties.[102-105] In this context, playing with the redox activity of TTF-based lanthanide SMMs seems very promising but until now the isolated species involved the TTF core in its neutral oxidation state and the examples of lanthanide coordination complexes involving the TTF core in its radical cation oxidation state are very rare.[106,107] Only few examples related the effect of the oxidation of the TTF core on the physical properties.[108,109] Very recently, some of us studied the different oxidation states of the redox-active dysprosium SMM **5** by spectro-electrochemistry and computational approaches.[110] The effect of the oxidation of **L^2** was studied on the structural, optical and magnetic properties. The optimized molecular structures were determined by DFT calculations revealing that oxidation led to an increase of the central C=C bond length and a disappearance of the boat conformation of the TTF fragment (Figure 8a) due to the increase of the aromaticity character from neutral to radical cation to dicationic oxidation state.

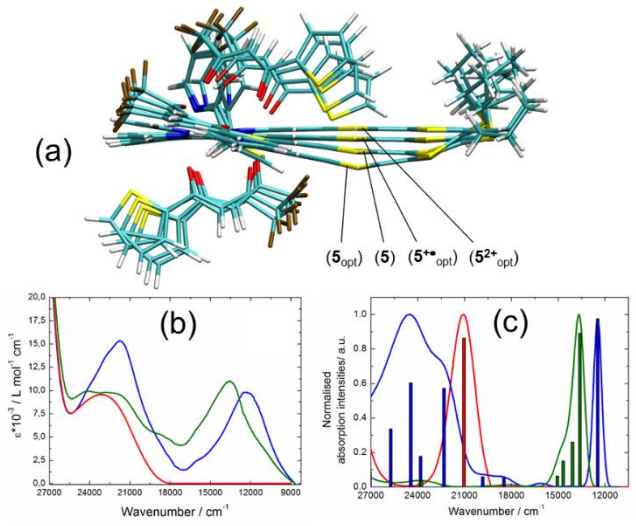

Figure 8. (a) Experimental X-ray structure of **5** and optimized structures for the different oxidation states $\mathbf{5}_{opt}$, $\mathbf{5}^{+\bullet}_{opt}$ and $\mathbf{5}^{2+}_{opt}$. Color code: carbon: turquoise, nitrogen: blue, oxygen: red, Sulphur: yellow, fluoride: brown and hydrogen: white. (b) Experimental absorption spectra for **5** (red curve), $\mathbf{5}^{+\bullet}$ (blue curve) and $\mathbf{5}^{2+}$ (green curve), (c) theoretical absorption spectra for $\mathbf{5}_{opt}$ (red curve), $\mathbf{5}^{+\bullet}_{opt}$ (blue curve) and $\mathbf{5}^{2+}_{opt}$ (green curve), the bars represent the mean contribution of the absorption spectra. Adapted from ref [110].

The decrease of the electron density on the TTF core slightly affected the coordination sphere of the Dy(III) center with Dy-N and Dy-O distances respectively lengthened and shortened after oxidation. The effect of the oxidation on the optical properties was drastic with a full change of the absorption spectra in the visible range (Figure 8b). The electronic transitions responsible for the red, blue and green colors of the respective **5**, $\mathbf{5}^{+\bullet}$ and $\mathbf{5}^{2+}$ complexes were identified by TD-DFT calculations (Figure 8c). For **5**, The transition centered at 21000 cm^{-1} is due to the ILCT HOMO → LUMO from the TTF to bzip fragments excitations. After the first single-electron oxidation, the electronic excitation spectrum of $\mathbf{5}^{+\bullet}$ highlighted two set of transitions at 12500 cm^{-1} attributed to Intra-Donor (ID) HOMO-3β → LUMOβ and at 22300 cm^{-1} and 24500 cm^{-1} due to ILCT HOMOα → LUMOα from the $TTF^{+\bullet}$ to bzip fragments. Finally, after the second single-electron oxidation, the electronic excitation spectrum of $\mathbf{5}^{2+}$ in the visible range is composed of several transitions ranging from 13000 cm^{-1} to 15000 cm^{-1} and mainly attributed to ILCT HOMO-5/-6 → LUMO from tta^- to TTF^{2+} excitations. It is worth to notice that such latter excitations are possible because after two single electron oxidation the dicationic TTF^{2+} specie is not any more a good electron donor but can be seen as an electron acceptor compared to the tta^- anion.

In a molecular point of view, the oxidation of the TTF fragment did not significantly affect the magnetic properties. In the three oxidation states, the energy splitting of the $^6H_{15/2}$ ground state, Ising character and the orientation of the anisotropy axis remain almost identical. Such preliminary results demonstrated the possibility to oxidize the TTF fragment without deterioration of the SMM behavior and thus are promising to the aim of designing conducting SMMs.

Paramagnetic Tetrathiafulvalene-based Ligand

A very challenging synthetic route is the design of TTF core functionalized with stable organic radical (S = ½) able to realize coordination reaction with metal centers. Such strategy is promising because the organic radical plays the magnetic relay between the π mobile electrons and the paramagnetic metal. In addition, SMMs involving lanthanide coordinated to organic radicals have highlighted promising magnetic properties with high blocking temperature due to the positive effect of the magnetic interaction between the 4f electrons and the organic radicals.[111-117] Due to the very high difficulty level of this kind of chemistry, only few researchers succeeded to combine TTF core with stable organic radical and no example of coordination with metal centers were reported.[118-127] A new TTF-Nitronyl Nitroxide (NIT) 2-{1-[methylbenzo(1-oxyl-3-oxide-4,4,5,5-tetramethylimidazoline)]-4,5-[4,5-bis(propylthio)-tetrathiafulvalenyl]-1H-benzimidazol-2-yl}pyridine triad (**L³**) (Scheme 1) was successfully designed by alkylating the molecular skeleton **L¹** with the 4-bromomethylbenzo(1-oxyl-3-oxide-4,4,5,5-tetramethylimidazolin-2-yl) radical[128-130] in DMF at room temperature in presence of K_2CO_3 as the base. The X-ray structure confirmed the expected dyad with the molecular platform alkylated with the nitronyl nitroxide (Figure 9a).[131] The crystal packing revealed the dimerization of the NIT radical as well as head-to-tail dimers of the TTF platforms.

The electrochemical properties shown three reversible mono-electronic oxidation waves at 0.51 V, 0.84 V and 0.93 V (Figure 9b). The first and third ones were attributed to the formation of the radical cation and dicationic forms of the TTF core while the second one is attributed to the formation of the oxoammonium cation form of the NIT arm. Interestingly cyclic voltammetry attested the possibility to oxidize the TTF core in its radical cation oxidation state maintaining the integrity of the NIT radical.

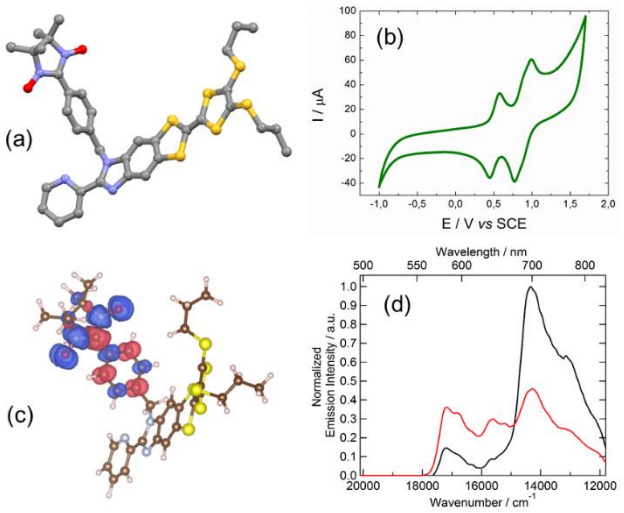

Figure 9. (a) X-ray structure of **L³**. Color code: carbon: grey, nitrogen: blue, oxygen: red and Sulfur: yellow. (b) Cyclic voltamogram of **L³** in CH_2Cl_2 at a scan rate of 100 mV s^{-1}. The potentials were measured versus a saturated calomel electrode (SCE) with Pt wires as working and counter electrodes. (c) Spin density distribution with Mulliken analysis spin population (spin cut off 0.0005 e^- $bohr^{-3}$). (d) Solution luminescence spectra of **L³** in CH_2Cl_2 (C = 1.9 × 10^{-5} M) at 77 K (λ_{ex} = 27027 cm^{-1} (370 nm) in the intra-NIT excitation for the black curve and λ_{ex} = 23810 cm^{-1} (420 nm) in the Intra-Ligand Charge Transfer for the red curve). Adapted from ref [131].

The integrity of the organic radical (S = ½) and its localization in **L³** was confirmed by calculating the total spin density distribution (Figure 9c). The Single-Occupied Molecular orbital (SOMO) is mainly localized on the 1-oxyl-3-oxide-imidazoline unit as expected. This result is in agreement with the room temperature EPR of **L³** which is characteristic of a single electron spin with g = 2.00716 coupled to two equivalent ^{14}N nuclear spins (a_N = 7.44 G).[132]

Finally the photo-physical properties of the **L³** triad were studied. Especially in an emission point of view, its spectrum is composed of several contributions attributed for the high-energy part (18000 – 15000 cm^{-1}) to the phosphorescence of the molecular TTF skeleton[56] while the low-energy part (12000 – 15000 cm^{-1}) was attributed to the emission of the NIT arm. The ratio of the two emissions could be modulated depending on the nature of the irradiated absorption band i.e. irradiation at high energy (27027 cm^{-1}) in the intra-NIT HOMO-1_α → $LUMO_\alpha$ and

HOMO-1_β → $LUMO_\beta$ transitions favors the emission of the NIT arm while an irradiation at lower energy (23810 cm^{-1}) in the ILCT (from TTF to bzip) favors the phosphorescence of the molecular TTF platform. The observation of the multi-emission for **L³** is possible because of the weak internal conversion between the excited singlet states on both NIT radical and molecular TTF-based skeleton.[133] **L³** is one of the rare examples of triad involving a stable organic radical and to the best of our knowledge the unique example of triad involving a TTF donor and two different acceptors, whose one is a NIT fragment, suitable for coordination reaction and possible design of multifunctional systems. The coordination reactions of **L³** with several lanthanide precursors are under progress in our laboratory but no results were published yet on them.

Auto-assembly of Single-Molecule Magnet

This section is dedicated to the design of polynuclear systems able to display multi-SMM behavior. To reach this aim, the alkylated arm must be suitable for the coordination with metal precursors. The first ligand of this section was design by alkylation of the molecular TTF-based skeleton **L¹** with the 4-(bromomethyl)-4'-methyl-2,2'-bipyridine[134] in DMF at 70 °C in presence of K_2CO_3 as the base. The resulting ligand 2-{1-[4,4'-dimethyl-2,2'-bipyridyl]-4,5-[4,5-bis(propylthio)-tetrathiafulvalenyl]-1H-benzimidazol-2-yl}pyridine (**L⁴**) was reacted with 2 equivalents of $Dy(hfac)_3{\cdot}2H_2O$ precursors leading to the formation of the $[(Dy_2(hfac)_6(\mathbf{L^4})]{\cdot}CH_2Cl_2$ (**6**) compound.[135]

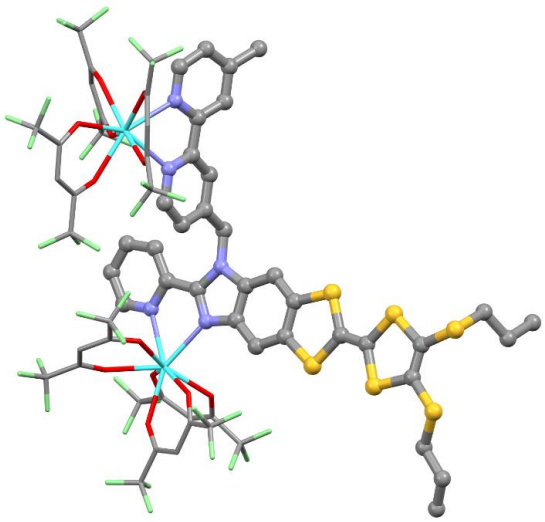

Figure 10. X-ray structure of $[(Dy_2(hfac)_6(\mathbf{L^4})]{\cdot}CH_2Cl_2$ (**6**). Ligand **L⁴** is represented in ball and sticks and the $Dy(hfac)_3$ fragment is represented in capped sticks. Color code: carbon: grey, nitrogen: blue, oxygen: red, Sulfur: yellow, fluoride: light green and dysprosium: light blue. Adapted from ref [135].

The X-ray structure confirmed the coordination of the $Dy(hfac)_3$ moieties to both bipyridine and imidazole-2-pyridine coordination sites (Figure 10). The symmetry of the coordination sphere is close to D_{4d} for both Dy(III) centers. Since the two coordination sites are similar and the arrangement of the coordinated ligands led to the same ideal D_{4d} symmetry around the Dy(III), the dynamical magnetic properties could not be distinguished for each lanthanide and it was considered that the two Dy(III) ions relaxed at the same rate. Indeed, the ac measurement under 800 Oe applied magnetic field displayed a single Gaussian response (Figure 11a) but it was in agreement with the magnetic contribution for two Dy(III) ions. The thermal variation of the relaxation time of the magnetization followed an Orbach regime at the highest temperature (above 6 K, red line on Figure 11b) ($\tau_0 = 3.7(1) \times 10^{-7}$ s and $\Delta = 39.6(2)$ cm^{-1}) but can be fitted with only a Raman process $\tau = C \times T^n$ with $C = 4.8(6) \times 10^{-3}$ and n = 6.26(7). The value of n is close to the expected value for Kramer's ions.[136,137] The magnetic relaxation in **6** was slow enough to observe a magnetic bistability for a non-zero magnetic field (Figure 11c). The predominance of the Raman process was confirmed by the calculated energy barrier of 90 cm^{-1} which is twice the experimental value, an indication that under-barrier mechanisms, such as Raman process, are operating in the magnetic relaxation.

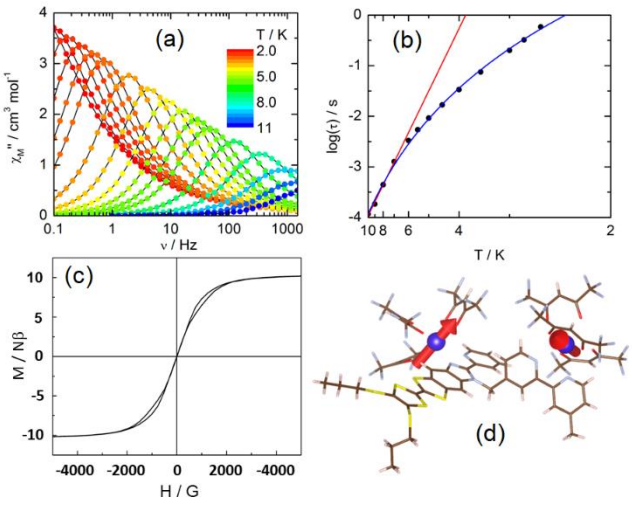

Figure 11. (a) Frequency dependence of χ_M" between 2 and 10 K for **6**. (b) Temperature dependence of the relaxation time measured in an applied magnetic field of 800 Oe with best fitted curves (in red for Orbach, in blue for Raman) in the temperature range of 2.5-10 K. (c) Magnetic hysteresis loop of **6** at 0.47 K. (d) Representation of the theoretical orientations of the main component of the ground state anisotropy tensor for the two Dy(III) centers in **6**. Adapted from ref [135].

Ab initio calculations confirmed that the two Dy(III) centers are magnetically similar since the ground state were characterized by the magnetic anisotropy tensor $g_z = 19.24$ and $g_z = 19.34$ while g_x and g_y are negligible. The easy axis for each metal center is oriented perpendicular to the plane formed by the two nitrogen atoms of the coordination site i.e. along the most

charged direction in agreement with the Oblate character of the dysprosium (Figure 11d).

The ligand **L⁴** proposed two similar coordination sites leading to a dinuclear system which displayed SMM behavior but without magnetic distinction between the two metal centers. Thus the next step consisted in the disymmetrisation of the two coordination sites. The ligands 2-(1-(2,6-di(pyrazol-1-yl)-4-methylpyridyl)-4,5-(4,5-bis(propylthio)-tetrathiafulvalenyl)-1H-benzimidazol-2-yl)-pyridine (**L⁵**) and 2-(1-(4'-[4-(methylphenyl)]-2,2:6',2"-terpyridyl)-4,5-(4,5-bis(propylthio)-tetrathiafulvalenyl)-1H-benzimidazol-2-yl)-pyridine (**L⁶**) (Scheme 1) were obtained by alkylation of **L¹** with the 2,6-di(pyrazol-1-yl)-4-(bromomethyl)pyridine[138,139] and 4'-[4-(bromomethyl)phenyl]-2,2:6',2"-terpyridine[140] using similar procedure than for **L⁴**. Once they reacted with two equivalents of $Dy(hfac)_3{\cdot}2H_2O$ precursors, dinuclear complexes were obtained and isolated as single crystals with the formula $[Dy_2(hfac)_6(\mathbf{L^5})]\cdot(CH_2Cl_2)_2\cdot C_6H_{14}$ (**7**)[141] and $[Dy_2(hfac)_6(L_6)]\cdot C_6H_{14}$ (**8**)[142] (Figure 12).

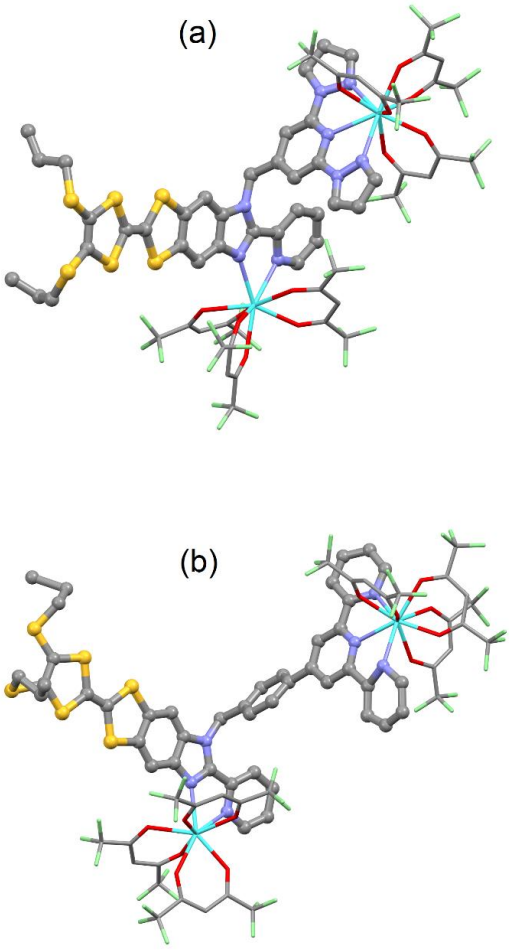

Figure 12. X-ray structures of (a) $[Dy_2(hfac)_6(\mathbf{L^5})]\cdot(CH_2Cl_2)_2\cdot C_6H_{14}$ (**7**) and (b) $[Dy_2(hfac)_6(\mathbf{L^6})]\cdot C_6H_{14}$ (**8**). Ligands **L⁵** and **L⁶** are represented in ball and sticks and the $Dy(hfac)_3$ fragment is represented in capped sticks. Color code: carbon: grey, nitrogen: blue, oxygen: red, Sulfur: yellow, fluoride: light green and dysprosium: light blue. Adapted from refs [141,142].

The two structures confirmed that the two bis- and tris-chelating coordination sites are occupied by the $Dy(hfac)_3$ moieties with distinct coordination sphere symmetry. The eight coordinated Dy(III) ions adopted a D_{4d} N2O6 surrounding in **7** and **8** while the nine coordinated Dy(III) ions adopted a D_{3h} N3O6 surrounding in **7** and a C_{4v} N3O6 surrounding in **8**. The modification of symmetry around the metal center led to subtle changes in the dynamic magnetic properties between the two dinuclear complexes but also between the two metal centers within the same complex. The dynamic magnetic properties of **7** revealed the appearance of an out-of-phase contribution of the magnetic susceptibility at high frequency but without maximum due to the efficiency of the QTM. Thus an optimal applied magnetic field of 1500 Oe is applied leading to a frequency dependence of the magnetic susceptibility with two contributions indication of a multi-relaxation mode (Figure 13a). Taking into account the particularity of the system **7**, such magnetic behavior was associated to the presence of two crystallographically different dysprosium ions.[143-147] From the previous magnetic investigation on the compounds **2** and **6**, the low frequency set of data was attributed to the eight coordinated Dy(III) ion in D_{4d} symmetry and consequently the high frequency set of data was attributed to the nine coordinated Dy(III) ion in D_{3h} symmetry.

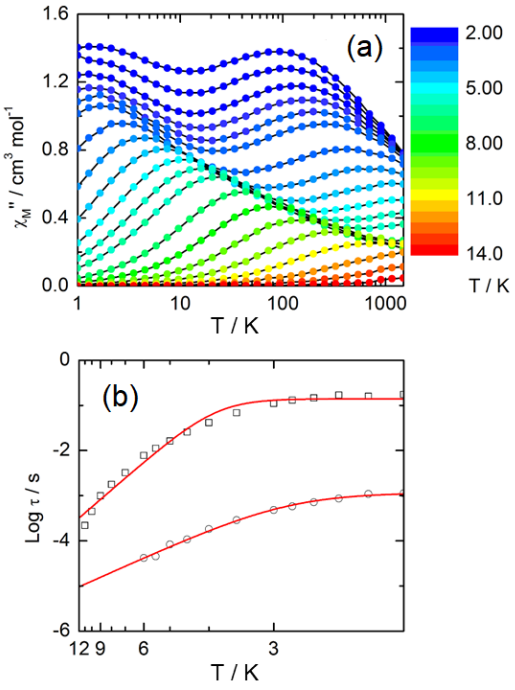

Figure 13. (a) Frequency dependence of χ_M" between 2 and 14 K for of **7** in an applied field of 1500 Oe. (b) Temperature dependency of the magnetic relaxation times (τ) at 1500 Oe for **7** in the temperature range of 2-12 K. Squares and open circles correspond to the data for the Dy(III) in eight and nine coordination number respectively. Red lines are the best-fit curves with modified Arrhenius law. Adapted from ref [141].

An extended Debye model was used to extract the relaxation time of the two dysprosium sites where χ_T and χ_S are the low- and high-

frequency limits of susceptibility, respectively, τ_i terms are the relaxation times and α_i terms the distributions of the relaxation time for the D_{4d} Dy(III) and C_{4v} Dy(III) sites, and β is the percentage of the susceptibility relaxing at τ_1. The Arrhenius law was drawn for each Dy sites (Figure 13b) and can be fitted by a combination of Orbach and remaining QTM with the following characteristic dynamic parameters Δ = 18(0.9) K, τ_0 = 2.15(40)×10^{-6} s and τ_{TI} = 1.17(9)×10^{-3} s for the D_{4d} Dy(III) ion and Δ = 5(3) K, $\tau 0$ = 1.8(6)×10^{-5} s and τ_{TI} = 0.14(2) s for the D_{3h} Dy(III) ion.

$$\chi_M' = \chi_S + (\chi_T - \chi_S)\left\{\frac{\beta\left[1+(\omega\tau_1)^{1-\alpha_1}\sin\left(\frac{\pi}{2}\alpha_1\right)\right]}{1+2(\omega\tau_1)^{1-\alpha_1}\sin\left(\frac{\pi}{2}\alpha_1\right)+(\omega\tau_1)^{2(1-\alpha_1)}} + \frac{(1-\beta)\left[1+(\omega\tau_2)^{1-\alpha_2}\sin\left(\frac{\pi}{2}\alpha_2\right)\right]}{1+2(\omega\tau_2)^{1-\alpha_2}\sin\left(\frac{\pi}{2}\alpha_2\right)+(\omega\tau_2)^{2(1-\alpha_2)}}\right\}$$

$$\chi_M'' = (\chi_T - \chi_S)\left\{\frac{\beta\left[(\omega\tau_1)^{1-\alpha_1}\cos\left(\frac{\pi}{2}\alpha_1\right)\right]}{1+2(\omega\tau_1)^{1-\alpha_1}\sin\left(\frac{\pi}{2}\alpha_1\right)+(\omega\tau_1)^{2(1-\alpha_1)}} + \frac{(1-\beta)\left[(\omega\tau_2)^{1-\alpha_2}\cos\left(\frac{\pi}{2}\alpha_2\right)\right]}{1+2(\omega\tau_2)^{1-\alpha_2}\sin\left(\frac{\pi}{2}\alpha_2\right)+(\omega\tau_2)^{2(1-\alpha_2)}}\right\}$$

The discrimination between the two lanthanide centers is also possible by looking at the emission properties for the Yb(III) analogue.[135] In fact the NIR emission spectrum of the Yb(III) analogue has been found to be the combination of two emission spectra of previously studied compounds in which the Yb(III) ion adopted only a D_{4d} N2O6 environment[56] or only a D_{3h} N3O6 environment.[133] Nevertheless the two Yb(III) ions gave the same $^2F_{5/2}$ excited state life time of 11.9 μs.

The second dinuclear [Dy_2(hfac)$_6$(**L^6**)]·C_6H_{14} complex (**8**) behaved as an SMM with a very similar frequency dependence of the magnetic susceptibility than for **7**. The high and low frequency sets of data were respectively attributed to the C_{4v} N3O6 (green plots on Figure 14a) and D_{4d} N2O6 (blue plots on Figure 14a) dysprosium centres. Ab initio calculations indicated a strong uniaxial magnetic anisotropy (g_z = 19.61 and 19.68) as well as the same orientation of the anisotropy axis for both metal ions. The molecular electrostatic potential around each Dy(III) ions was plotted using the home-made CAMMEL software (Calculated Molecular Multipolar Electrostatics) (Figure 14b). Such plots highlighted the preponderant contribution of the $hfac^-$ anions compared to the nitrogen in the crystal field[148] leading to similar energy splitting and calculated energy barriers for both Dy(III) ions (207 cm^{-1} and 178 cm^{-1}). At this point the ab initio calculations underlined similar magnetic properties in terms of magnetic anisotropy and ground state nature while the experience showed significant difference of magnetic relaxation time. The explanations were given by the fit of the Arrhenius law (Figure 14a).

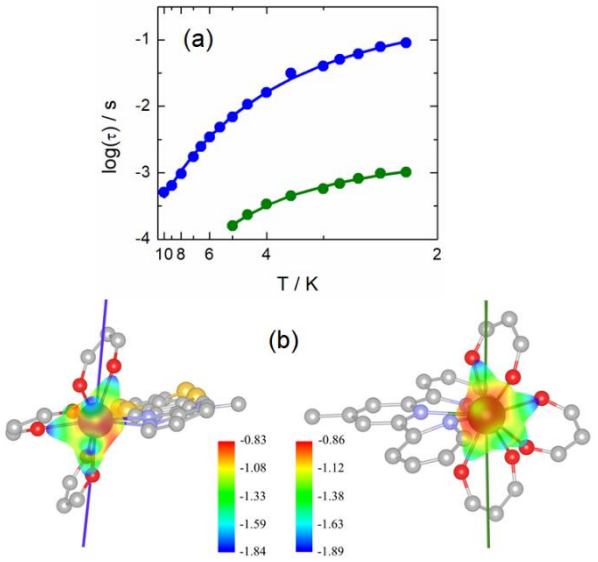

Figure 14. (a) Temperature dependence of the magnetic relaxation times (τ) at 3000 Oe for **8** in the temperature range of 2-10 K (blue disks) and 2-5 K (green disks) for Dy(III) in eight and nine coordination number respectively. Blue and green lines are the best fitted curves with parameters given in the text. (b) Orientation of the computed ground state g-tensor main component (g_z) and projection of the molecular electrostatic potential on the eight coordinated Dy(III) (left, blue line) and nine coordinated Dy(III) (right, green line) centers. Adapted from ref. [142].

While the magnetization of the D_{4d} Dy(III) ion mainly relaxed through a Raman process, the one for the C_{4v} Dy(III) ion mainly relaxed through a Direct process. Consequently the C_{4v} Dy(III) relaxed faster than the D_{4d} Dy(III) ion even if ground state nature and magnetic anisotropy are similar for both dysprosium centers.

In 2011, some of us used the tetrathiafulvalene-3-pyridine-*N*-oxide ligand (**L**) to design a dinuclear compound of formula [Dy(tta)$_3$(**L**)]$_2$·0.5CH_2Cl_2 (**9**) (Figure 15a).[149] The pyridine-3-oxide allowed the bridging of the two Dy(III) centres leading to a significant magnetic interaction of J = -2.30 cm^{-1} and g = 19.2 (simulation performed at low temperature regime in a Ising pattern with an effective spin S = ½ and an anisotropic g tensor).[150] **9** behaved as an SMM with a magnetic relaxation through an Orbach process (τ_0 = 5.48(4) × 10^{-7} s and Δ = 87(1) K) above 10 K. Magnetization loops at 0.48 K revealed a double butterfly-like hysteresis with a small coercive field associated to the presence of antiferromagnetic interaction and QTM at the single-ion level (Figure 15b). The hysteresis loop narrowed at 1600 Oe because the level crossing between the first excited and ground states of the dimer which opens a new tunnel of the magnetization in accelerating the relaxation process.[151-157] By using the Ising approximation with the following equation $H_{crossing} = -J/2g\beta$ and the

previously determined parameters, the theoretical value of the $H_{crossing}$ should be 1300 Oe which is in agreement with the observed value.

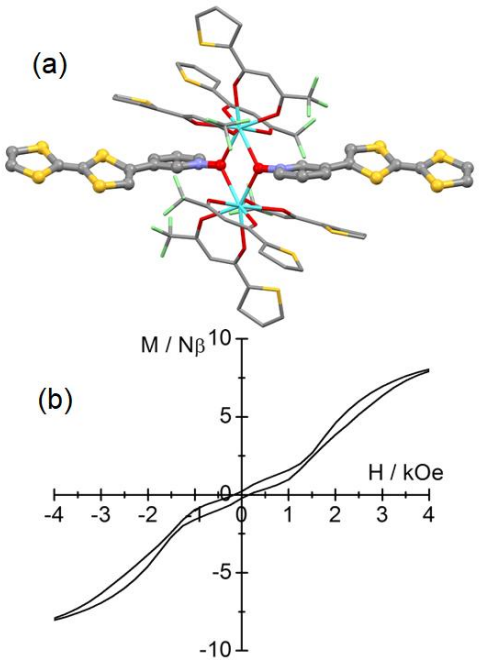

Figure 15. (a) X-ray structure of the dinuclear complex $[Dy(tta)_3(\mathbf{L})]_2{\cdot}0.5CH_2Cl_2$ (**9**). Color code: carbon: grey, nitrogen: blue, oxygen: red, Sulfur: yellow, fluoride: light green and dysprosium: light blue. (b) Magnetic hysteresis loop at 0.48 K and a sweep rate of 16 Oe s^{-1} for **9**. Ligand **L** is represented in ball and sticks and the $Dy(tta)_3$ fragment is represented in capped sticks. Adapted from ref. [149].

At this point of the review, the readers have seen that the mononuclear $[Dy(tta)_3(\mathbf{L^2})]{\cdot}C_6H_{14}$ complex (**5**) displayed a butterfly-like hysteresis without remnant magnetization but quite strong coercitive field for non-zero applied field while the dinuclear $[Dy(tta)_3(\mathbf{L})]_2{\cdot}0.5CH_2Cl_2$ complex (**9**) presented a double butterfly-like hysteresis with a remnant field but small coercive field under an applied field. The obvious question was then can we combine the advantages of **5** and **9** in an unique system to observe an hysteresis loop with both remnant magnetization and an coercive field? To reach such objective, the 2-{1-methylpyridine-N-oxide-4,5-[4,5-bis(propylthio)tetrathiafulvalenyl]-1H-benzimidazol-2-yl}pyridine ligand ($\mathbf{L^7}$) (Scheme 1) was designed. It combined the two required coordination sites i.e. the bischelating benzimidazol-2-pyridine and pyridine-4-oxide fragments. As predicted the association of $\mathbf{L^7}$ with two equivalents of $Dy(tta)_3{\cdot}2H_2O$ precursor led to the rational design of the tetranuclear $[Dy_4(tta)_{12}(\mathbf{L^7})_2]{\cdot}(C_6H_{14})_4$ complex (**10**) (Figure 16).[158] The tetranuclear complex **10** is composed of two external Dy(III) ions linked to the bischelating coordination site of the common molecular skeleton. Then the two external mononuclear fragments are bridged by a dinuclear specie formed by two $Dy(tta)_3$ units linked through two 4-pyridine-N-oxide bridges (Figure 16). In other words, **10** can be structurally seen like two mononuclear complexes **5** bridge by a dinuclear complex **9** demonstrated the success of the chemical approach.

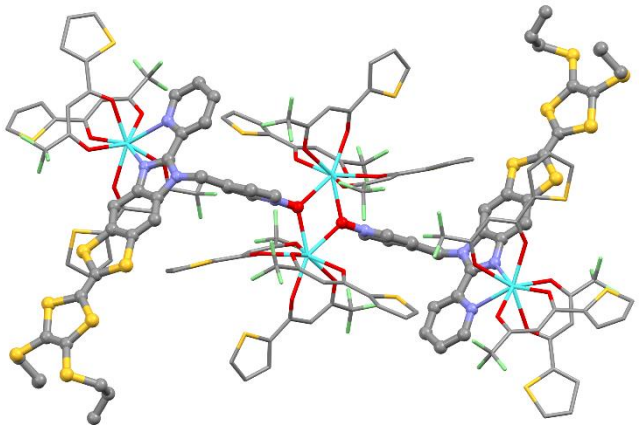

Figure 16. X-ray structure of the tetranuclear $[Dy_4(tta)_{12}(\mathbf{L^7})_2]{\cdot}(C_6H_{14})_4$ complex (**10**). Ligand $\mathbf{L^7}$ is represented in ball and sticks and the $Dy(tta)_3$ fragment is represented in capped sticks. Color code: carbon: grey, nitrogen: blue, oxygen: red, Sulfur: yellow, fluoride: light green and dysprosium: light blue. Adapted from ref. [158].

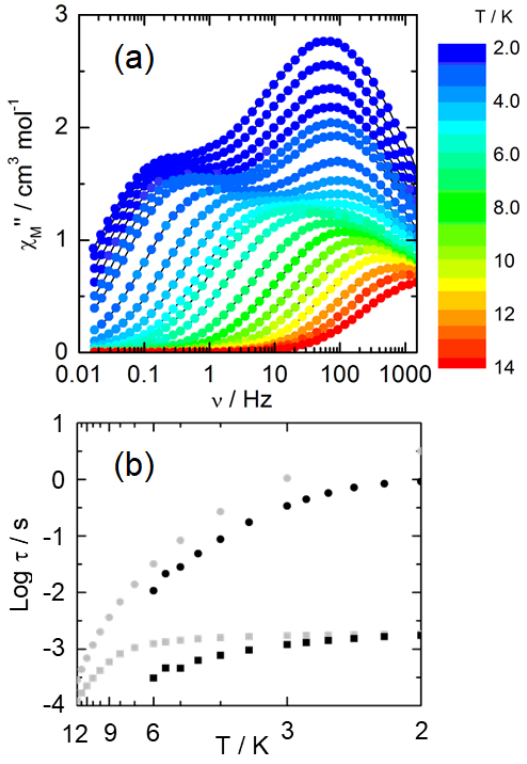

Figure 17. (a) Temperature and frequency dependence of the out-of-phase component of the ac susceptibility measured in zero applied magnetic field for **10**. (b) Temperature dependence of the slow (black disks) and fast (black squares) regimes of **10** measured in zero applied magnetic field. The thermal variation of the logarithm of the relaxation times for isolated **9** (grey disks) and **5** (grey squares) are represented for comparison. Adapted from ref. [158].

The ac magnetic measurements revealed SMM behavior with the out-of-phase component of the susceptibility which could be split in two set of data (Figure 17a). A slow regime highlighted a continuous thermally dependent behavior while the fast regime was almost thermally independent until 7 K. The slow regime was associated to the magnetic relaxation of the two central Dy(III) ions with a partial quenching of the QTM due to the antiferromagnetic interactions while the fast regime was associated to the two external Dy(III) ions. An extended Debye model was used to extract the magnetic relaxation time and represented the Arrhenius law for the two regimes (Figure 17b). Thus one can conclude that the slow and fast regimes coincided with the separated mononuclear **5** and dinuclear **9** respectively. Unfortunately the hysteresis loop was only slightly opened at 0.48 K without remnant magnetization. In fact the relaxation times for **10** are slightly shorter than those in isolated moieties. The effect of potential dipolar interaction cannot be rule out in the resulting faster magnetic relaxation times.

Chiral Single-Molecule Magnet

To close this review, a last example in which the property of chirality appeared is described. The aim is to study the effect of chirality on the SMM behaviour. To do so, some of us recently demonstrated that the magnetic behavior can be drastically modulated between the racemic form and a pure enantiomer of a dysprosium complex.[159] To go one step further, both highly optically active and redox active fragments were combined in a unique organic ligand where the former one was an [6]helicene[160] while the latter was the tetrathiafulvalene-based common molecular skeleton. These two fragments were previously assembled[161] but without opening the route of possible coordination reaction. The resulting ligand 2-{1-[2-methyl[6]helicene]-4,5-[4,5-bis(propylthio)tetrathiafulvalenyl]-1H-benzimidazol-2-yl}pyridine (**L^{8}**) gave the expected mononuclear [Dy(hfac)$_3$(**L^{8}**)]·0.5CH_2Cl_2 (**11**) (Figure 18a).[162] The X-ray structure of **11** revealed the alkylation of the TTF molecular skeleton with the 2-methyl[6]helicene arm as well as the coordination of the Dy(hfac)$_3$ unit to the imidazole-2-pyridine fragment. The ac measurements highlighted a field-induced SMM (H = 1000 Oe) with a magnetic relaxation through a Raman process ($\tau = CT^n$ with $C = 2.4(4) \times 10^{-2}$ and n = 5.5). Thanks to the triclinic P-1 space group of crystallization for **11**, the g tensor can be experimentally determined by measuring the magnetization of an oriented single crystal (Figure 18b). The experimental Ising value of g_z = 19.6 was confirmed by ab initio calculations (g_z = 19.09) and the composition of the ground state consists in 88 % $|\pm15/2\rangle$ and 10 % $|\pm11/2\rangle$ components. The first excited state was found 75 K above the ground state which is much smaller than the experimental energy barrier considering a pure Orbach process (21.1 K) and then confirming the magnetic relaxation through the under-barrier (Figure 18c) such as QTM (H = 0 Oe) and Raman processes. **11** is an unprecedented example of chiral redox-active lanthanide SMM and paves the way for the design of switchable-multi-property SMMs.

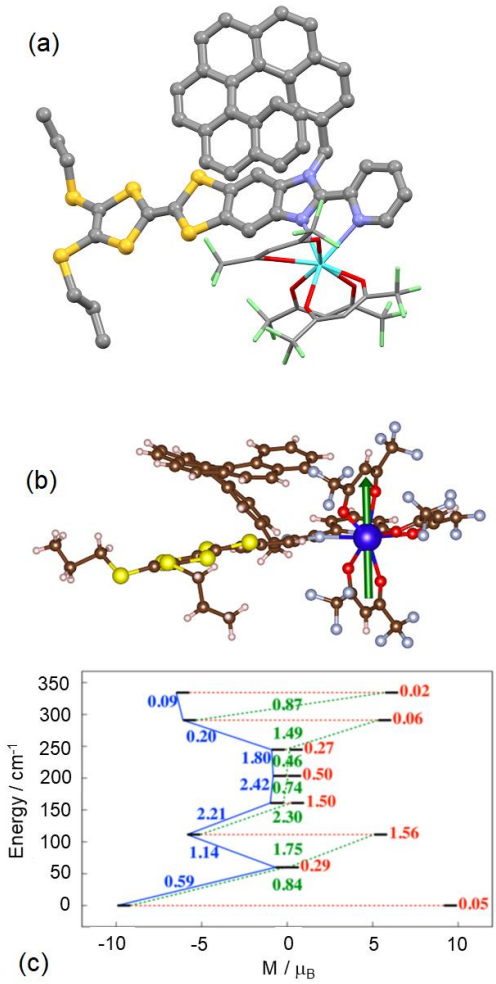

Figure 18. (a) X-ray structure of [Dy(hfac)$_3$(**L^{8}**)]·0.5CH_2Cl_2 (**11**). Ligand **L^{8}** is represented in ball and sticks and the Dy(hfac)$_3$ fragment is represented in capped sticks. Color code: carbon: grey, nitrogen: blue, oxygen: red, Sulfur: yellow, fluoride: light green and dysprosium: light blue. (b) Representation of the theoretical main anisotropy axis (green arrow). (c) Computed magnetization blocking barriers. The numbers provided are the mean absolute values for the corresponding matrix elements of the magnetic transition dipole moment. Adapted from Ref. [162].

Conclusions and Outlook

The TTF-based lanthanide complexes are not competitive in terms of blocking temperature but they are one of the most explored systems for multi-properties coordination compounds thanks to the redox-activity of the TTF-based ligands and the dual magnetic and optical properties of the lanthanide ions. Nevertheless, as demonstrated in this paper, starting from a common molecular TTF-based skeleton (the 2-(4,5-bis(propylthio)tetrathiafulvalenyl)-1H-benzimidazol-2-yl)-pyridine (**L^{1}**)), a library of TTF-based ligands could be obtained by alkylation of it with different chelating arms. Using all the usual experimental and computational approaches developed in molecular magnetism research field, the role of the supramolecular interaction in the switching of the SMM behavior

could be studied and more information about the role of the symmetry and electronic distribution of the coordination sphere around the lanthanide ion could be obtained doing simple molecular engineering i.e. replacing the $hfac^-$ with tta^- anions. One breakthrough was reached in 2015 when the role of the hyperfine interaction on the quantum tunneling of the magnetization was demonstrated on isotopically pure SMM. This result was then deepened in 2019 with the highlighting of the role of both nuclear spin value on the Raman process and the hyperfine constant values on the magnetic relaxation. Muon spin relaxation (μSR) was used to detect the slowing down of the zero-field magnetic relaxation as shown by SQUID magnetometry but μSR is sensitive to all fluctuation modes modulating the spin state lifetime and could be a helpful technique to probe the dynamics of molecules on a surface in the objective of designing quantum gates. The alkylation of **L^1** with specific chelating arms allowed the rational design of polynuclear systems with multi-SMM behavior as well as the rational assembly of SMMs. The different magnetic relaxation rates have been attributed to each different magnetic centers thanks to the identification of the magnetic relaxation processes operating for these centers in function of the symmetry and electronic distribution of their coordination sphere. Finally, paramagnetic and chiral alkylating arms have been grafting on the molecular skeleton.

The molecular magnetism field is now moving in two main directions with the design of high blocking temperature linear organometallic SMM and the spintronics/Qubits. The first route takes its source from the understanding of the previously studied SMMs of the literature and then how the magnetic anisotropy can be optimized while for the second direction lanthanide isotopes could play an important role since they can modulate both QTM and quantum coherence time. With these evolution in mind, TTF-based ligands can still play an import role with the design of coordination complexes which display magnetic interaction, spin crossover, circularly polarized luminescence and redox switching of both magnetic and optical behavior and grafting of such complexes on surface thank to the extended π system and thioalkyl groups[163]. These perspectives are under investigation in our laboratory.

Acknowledgements

This work was supported by the Université de Rennes 1, CNRS, Rennes Métropole, Region Bretagne, FEDER, Agence Nationale de la Recherche (N° ANR-13-BS07-0022-01) and the European Commission through the ERC-CoG 725184 MULTIPROSMM (project n. 725184). All the Master, PhD students and post-docs are warmly thanked for their essential contributions. Special thanks are addressed to S. Golhen, K. Bernot, Y. Le Gal, B. Lefeuvre (ISCR, Rennes, France) and F. Riobé, O. Maury (ENS de Lyon, France).

Keywords: Tetrathiafulvalene • Lanthanides • Molecular Design • Single-Molecule Magnet • Photo-physical properties

[1] F. Wudl, D. Wobschall, E. J. Hufnagel, *J. Am. Chem. Soc.* **1972**, *94*, 670-672.
[2] H. Kobayashi, A. Kobayashi, P. Cassoux*, Chem. Soc. Rev.* **2000**, *29*, 325−333.
[3] E. Coronado, J. R. Galan-Mascaros, C. J. Gomez-Garcia, V. Laukhin, *Nature* **2000**, *408*, 447−449.
[4] H. Tanaka, H. Kobayashi, A. Kobayashi, P. Cassoux, *Adv. Mater.* **2000**, *12*, 1685-1689.
[5] S. Uji, H. Shinagawa, T. Terashima, C. Terakura, T. Yakabe, Y. Terai, M. Tokumoto, A. Kobayashi, H. Tanaka, H. Kobayashi, *Nature*, **2001**, *410*, 908-910.
[6] J. Yamada, T. Sugimoto, Ed. TTF Chemistry: Fundamentals and Tetrathiafulvalene; Kodansha-Springer: Tokyo, **2004**.
[7] M. Bendikov, F. Wudl, D. F. Perepichka, *Chem. Rev.* **2004**, *104*, 4891−4945.
[8] A. Gorgues, P. Hudhomme, M. Sallé, *Chem. Rev.* **2004**, *104*, 5151−5184.
[9] F. Pointillart, S. Golhen, O. Cador, L. Ouahab, *Dalton Trans*. **2013**, *42*, 1949-1960.
[10] D. Lorcy, N. Bellec, M. Fourmigué, N. Avarvari, *Coord. Chem. Rev.* **2009**, *253*, 1398-1438.
[11] S. Faulkner, B. P. Burton-Pye, T. Khan, L. R. Martin, S. D. Wray, P. J. Skabara, *Chem. Commun.* **2002**, *16*, 1668-1669.
[12] F. Pointillart, Y. Le Gal, S. Golhen, O. Cador, L. Ouahab, *Inorg. Chem.* **2009**, *48*, 4631-4633.
[13] K. Kuriki, Y. Koike, Y. Okamoto, *Chem. Rev.* **2002**, *102*, 2347−2356.
[14] J.-C. G. Bünzli, *Chem. Rev.* **2010**, *110*, 2729−2755.
[15] R. M. Duke, E. B. Veale, F. M. Pfeffer, P. E. Kruger, T. Gunnlaugsson, *Chem. Soc. Rev.* **2010**, *39*, 3936−3953.
[16] E. G. Moore, A. P. S. Samuel, K. N. Raymond, *Acc. Chem. Res.* **2009**, *42*, 542−552 and references therein.
[17] A. Beeby, S. W. Botchway, I. M. Clarkson, S. Faulkner, A. M. Parker, D. Parker, J. A. G. Williams, *J. Photochem. Photobiol. B* **2000**, *57*, 83−89.
[18] J. H. van Vleck, *J. Phys. Chem.* **1937**, *41*, 67-80.
[19] D. Parker, *Coord. Chem. Rev.* **2000**, *205*, 109-130.
[20] D. Parker, *Chem. Soc. Rev.* **2004**, *33*, 156-165.
[21] J.-C. G. Bünzli, C. Piguet, *Coord. Chem. Rev.* **2005**, *34*, 1048-1077.
[22] S. V. Eliseeva, J.-C. G. Bünzli, *Chem. Soc. Rev.* **2010**, *39*, 189-227.
[23] F. Pointillart, T. Cauchy, O. Maury, Y. Le Gal, S. Golhen, O. Cador, L. Ouahab, *Chem. Eur. J.* **2010**, *16*, 11936-11941.
[24] F. Pointillart, A. Bourdolle, T. Cauchy, O. Maury, Y. Le Gal, S. Golhen, O. Cador, L. Ouahab, *Inorg. Chem.* **2012**, *51*, 978-984.
[25] A. D'Aléo, F. Pointillart, L. Ouahab, C. Andraud, O. Maury, *Coord. Chem. Rev.* **2012**, *256*, 1604-1620.
[26] D. Gatteschi, R. Sessoli, J. Villain, Molecular Nanomagnets; Oxford University Press: New York, NY, USA, 2006.
[27] L. Bogani, W. Wernsdorfer, *Nat. Mater.* **2008**, *7*, 179–186.
[28] M. Mannini, F. Pineider, P. Sainctavit, C. Danieli, E. Otero, C. Sciancalepore, A. M. Talarico, M.-A. Arrio, A. Cornia, D. Gatteschi, R. Sessoli*, Nat. Mater.,* **2009**, *8*, 194-197.
[29] M. N. Leuenberger, D. Loss, *Nature* **2001**, *410*, 789–793.
[30] J. Lehmann, A. Gaita-Arino, E. Coronado, D. Loss, *Nat. Nanotechnol*. **2007**, *2*, 312–317.
[31] M. Ganzhorn, S. Klyatskaya, M. Ruben, W. Wernsdorfer, Nat. Nanotechnol. **2013**, *8*, 165–169.
[32] N. Ishikawa, M. Sugita, T. Ishikawa, S. Y. Koshihara, Y. Kaizu, *J. Am. Chem. Soc.* **2003**, *125*, 8694-8695.
[33] F.-S. Guo, B.-M. Day, Y.-C. Chen, M.-L. Tong, A. Mansikkamäki, R.A. Layfield, *Angew. Chem., Int. Ed.* **2017**, *56*, 11445-11449.
[34] C. A. P. Goodwin, F. Ortu, D. Reta, N.F. Chilton, D. P. Mills, *Nature* **2017**, *548*, 439-442.
[35] K. R. McClain, C. A. Gould, K. Chakarawet, S. J. Teat, T.J . Groshens, J. R. Long, B. G. Harvey, *Chem. Sci.* **2018**, *9*, 8492-8503.
[36] F.-S. Guo, B.-M. Day, Y.-C. Chen, M.-L. Tong, A. Mansikkamäki, R. A. Layfield, *Science* **2018**, *362*, 1400-1403.

[37] F. Pointillart, B. Le Guennic, O. Cador, O. Maury, L. Ouahab, *Acc. Chem. Res.* **2015**, *48*, 2834-2842.

[38] C.-Y. Jia, S.-X. Liu, C. Tanner, C. Leiggener, L. Sanguinet, E. Levillain, S. Leutwyler, A. Hauser, S. Decurtins, *Chem. Commun.* **2006**, 1878-1880.

[39] C. Jia, S.-X. Liu, C. Tanner, C. Leiggener, A. Neels, L. Sanguinet, E. Levillain, S. Leutwyler, A. Hauser, S. Decurtins, *Chem. Eur. J.* **2007**, *13*, 3804-3812.

[40] G. Cosquer, F. Pointillart, S. Golhen, O. Cador, L. Ouahab, *Chem. Eur. J.* **2013**, *19*, 7895-7903.

[41] J. Jung, O. Cador, K. Bernot, F. Pointillart, J. Luzon, B. Le Guennic, *Beilstein J. Nanotechnol* **2014**, *5*, 2267-2274.

[42] F. R. Goncalves Silva, O. L. Malta, C. Reinhard, H. U. Güdel, C. Piguet, J.-E. Moser, J.-C. G. Bünzli, *J. Phys. Chem. A* **2002**, *106*, 1670−1677.

[43] M.-E., Boulon, G. Cucinotta, J. Luzon, C. Degl'Innocenti, M. Perfetti, K. Bernot, G. Calvez, A. Caneschi, R. Sessoli, *Angew. Chem., Int. Ed.* **2013**, *52*, 350−354.

[44] G. Cucinotta, M. Perfetti, J. Luzon, M. Etienne, P. E. Car, A. Caneschi, G. Calvez, K. Bernot, R. Sessoli, *Angew. Chem., Int. Ed.* **2012**, *51*, 1606−1610.

[45] J. Long, R. Vallat, R. A. S. Ferreira, L. D. Carlos, F. A. Almeida Paz, Y. Guari, J. Larionova, *Chem. Commun*. **2012**, *48*, 9974-9976.

[46] M. Ren, S.-S. Bao, R. A. S. Ferreira, L.-M. Zheng, L. D. Carlos, *Chem. Commun.* **2014**, *50*, 7621−7624.

[47] F. Pointillart, B. Le Guennic, T. Cauchy, S. Golhen, O. Cador, O. Maury, L. Ouahab, *Inorg. Chem.* **2013**, *52*, 5978−5990.

[48] F. Pointillart, B. Le Guennic, S. Golhen, O. Cador, O. Maury, L. Ouahab, *Chem. Commun.* **2013**, *49*, 615−617.

[49] M. Ren, S.-S. Bao, B.-W. Wang, R. A. S. Ferreira, L.-M. Zheng, L. D. Carlos, *Inorg. Chem. Front.* **2015**, *2*, 558-566.

[50] J. Long, E. Mamontova, V. Freitas, D. Luneau, V. Vieru, L. F. Chibotaru, R. A. S. Ferreira, G. Félix, Y. Guari, L. D. Carlos, J. Larionova, *RSC Adv.* **2016**, *6*, 108810-108818.

[51] K. Soussi, J. Jung, F. Pointillart, B. Le Guennic, B. Lefeuvre, S. Golhen, O. Cador, Y. Guyot, O. Maury, L. Ouahab, *Inorg. Chem. Front.* **2015**, *2*, 1105-1117.

[52] J. Long, Y. Guari, R. A. S. Ferreira, L. D. Carlos, J. Larionova, *Coord. Chem. Rev.* **201**8, *363*, 57-70.

[53] Y. Huo, Y.-C. Chen, S.-G. Wu, J.-L. Liu, J.-H. Jia, W.-B. Chen, B.-L. Wang, Y.-Q. Zhang, M.-L. Tong, *Inorg. Chem*. **2019**, *58*, 1301-1308.

[54] G. Brunet, R. Marin, M. Monk, U. resch-Genger, D. A. Galico, F. A. Sigoli, E. A. Suturina, E. Hemmer, M. Murugesu, *Chem. Sci.* **2019**, *10*, 6799-6808.

[55] J.-H. jia, Q.-W. Li, Y.-C. Chen, J.-L. Liu, M.-L. Tong, *Coord. Chem. Rev.* **2019**, *378*, 365-381.

[56] G. Cosquer, F. Pointillart, J. Jung, B. Le Guennic, S. Golhen, O. Cador, Y. Guyot, A. Brenier, O. Maury, L. Ouahab, *Eur. J. Inorg. Chem.* **2014**, 69-82.

[57] A. Abragam, B. Bleaney, *Electron Paramagnetic Resonance of Transition Ions*, Dover Publications, New York, **1986**.

[58] R. Orbach, *Proc. Phys. Soc. London Sect. A* **1961**, *264*, 458-495.

[59] C. Rudowicz, *J. Phys. C: Solid State Phys.* **1985**, *18*, 1415-1430.

[60] S. J. A. Pope, B. P. Burton-Pye, R. Berridge, T. Khan, P. Skabara, S. Faulkner, *Dalton Trans.* **2006**, 2907-2912.

[61] T. Lazarides, M. A. H. Alamiry, H. Adams, S. J. A. Pope, S. Faulkner, J. A. Weinstein, M. D. Ward, *Dalton Trans.* **2007**, 1484-1491.

[62] W. D. Horrocks Jr., J. P. Bolender, W. D. Smith, R. M. Supkowski, *J. Am. Chem. Soc.* **1997**, *119*, 5972-5973.

[63] R. M. Supkowski, J. P. Bolender, W. D. Smith, L. E. L. Reynolds, W. D. Horrocks Jr., *Coord. Chem. Rev.* **1999**, *185–186*, 307-319.

[64] A. Beeby, S. Faulkner, J. A. G. Williams, *J. Chem. Soc., Dalton Trans.* **2002**, 1918-1922.

[65] T. Lazarides, N. M. Tart, D. Sykes, S. Faulkner, A. Barbieri, M. D. Ward, *Dalton Trans.* **2009**, 3971-3979.

[66] F. Habib, G. Brunet, V. Vieru, I. Korobkov, L. F. Chibotaru, M. Murugesu, *J. Am. Chem. Soc.* **2013**, *135*, 13242-13245.

[67] F. Habib, P.-H. Lin, J. Long, I. Korobkov, W. Wernsdorfer, M. Murugesu, *J. Am. Chem. Soc.* **2011**, *133*, 8830-8833.

[68] S. Thiele, F. Balestro, R. Ballou, S. Klyatskaya, M. Ruben, W. Wernsdorfer, *Science* **2014**, *344*, 1135 – 1138.

[69] W. Wernsdorfer, A. Caneschi, R. Sessoli, D. Gatteschi, A. Cornia, V. Villar, C. Paulsen, *Phys. Rev. Lett.* **2000**, *84*, 2965 – 2968.

[70] F. Luis, M. J. Martinez-Pérez, O. Montero, E. Coronado, S. Cardona-Serra, C. Marti-Gastaldo, J. M. Clemente-Juan, J. Sesé, D. Drung, T. Schurig, *Phys. Rev. B* **2010**, *82*, 060403.

[71] Y. Kishi, F. Pointillart, B. Lefeuvre, F. Riobé, B. Le Guennic, S. Golhen, O. Cador, O. Maury, H. Fujiwara, L. Ouahab, *Chem. Commun*. **2017**, *53*, 3575-3578.

[72] E. Moreno-Pineda, M. Damjanovic, O. Fuhr, W. Wernsdorfer, M. Ruben, *Angew. Chem. Int. Ed.* **2017**, *56*, 9915-9919.

[73] Y.-C. Chen, J.-L. Liu, W. Wernsdorfer, D. Liu, L. F. Chibotaru, X.-M. Chen, M.-L. Tong, *Angew. Chem. Int. Ed.* **2017**, *56*, 4996-5000.

[74] G. Huang, X. Yi, J. Jung, O. Guillou, O. Cador, F. Pointillart, B. Le Guennic, K. Bernot, *Eur. J. Inorg. Chem.* **2018**, 326-332.

[75] F. Ortu, D. Reta, Y.-S. Ding, C. A. P. Goodwin, M. P. Gregson, E. J. L. McInnes, R. E. P. Winpenny, Y.-Z. Zheng, S. T. Liddle, D. P. Mills, N. F. Chilton, *Dalton Trans.* **2019**, *48*, 8541-8545.

[76] E. Moreno-Pineda, G. Taran, W. Wernsdorfer, M. Ruben, *Chem. Sci.* **2019**, *10*, 5138-5145.

[77] F. Pointillart, J. Jung, R. Berraud-Pache, B. Le Guennic, V. Dorcet, S. Golhen, O. Cador, O. Maury, Y. Guyot, S. Decurtins, S.-X. Liu, L. Ouahab, *Inorg. Chem.* **2015**, *54*, 5384-5397.

[78] P. Zhang, L. Zhang, C. Wang, S. Xue, S.-Y. Lin, and J. Tang, *J. Am. Chem. Soc.*, **2014**, *136*, 4484- 4487.

[79] A. J. Brown, D. Pinkowicz, M. R. Saber, and K. R. Dunbar, *Angew. Chem. Int. Ed.*, **2015**, 54, 5864- 5868.

[80] T. T. da Cunha, J. Jung, M.-E. Boulon, G. Campo, F. Pointillart, C. L. M. Pereira, B. Le Guennic, O. Cador, K. Bernot, F. Pineider, S. Golhen, L. Ouahab, *J. Am. Chem. Soc.* **2013**, *135*, 16332-16335.

[81] C. Dekker, A. F. M. Arts, H. W. Wijn, A. J. van Duyneveldt and J. A. Mydosh, *Phys. Rev. B: Condens. Matter*, **1989**, *40*, 11243–11251.

[82] M. A. Palacios, J. Nehrkorn, E. A. Suturina, E. Ruiz, S. Gomez-Coca, K. Holldack, A. Schnegg, J. Krzystek, J. M. Moreno, E. Colacio, *Chem. Eur. J.* **2017**, *23*, 11649 – 11661.

[83] E. Colacio, J. Ruiz, E. Ruiz, E. Cremades, J. Krzystek, S. Carretta, J. Cano, T. Guidi, W. Wernsdorfer, E. K. Brechin, *Angew. Chem. Int. Ed.* **2013**, *52*, 9130-9134.

[84] J.-L. Liu, K. Yuan, J.-D. Leng, L. Ungur, W. Wernsdorfer, F.-S. Guo, L. F. Chibotaru, M.-L. Tong, *Inorg. Chem.* **2012**, 51, 8538-8544.

[85] E. J. L. McInnes, E. Pidcock, V. S. Oganesyan, M. R. Cheesman, A. K. Powell, A. J. Thomson, *J. Am. Chem. Soc.* **2002**, *124*, 9219-9228.

[86] L. Bogani, L. Cavigli, M. Gurioli, R. L. Novak, M. Mannini, A. Caneschi, F. Pineider, R. Sessoli, M. Clemente-Leon, E. Coronado, A. Cornia, D. Gatteschi, *Adv. Mater.* **2007**, *19*, 3906-3911.

[87] R. L. Novak, F. Pineider, C. De Julian Fernandez, L. Gorini, L. Bogani, C. Danieli, L. Cavigli, A. Cornia, R. Sessoli, *Inorg. Chim. Acta* **2008**, *361*, 3970-3974.

[88] J. Jung, T. T. da Cunha, B. Le Guennic, F. Pointillart, C. L. M. Pereira, J. Luzon, S. Golhen, O. Cador, O. Maury, L. Ouahab, *Eur. J. Inorg. Chem.* **2014**, 3888-3894.

[89] Y. Bi, Y.-N. Guo, L. Zhao, Y. Guo, S.-Y.; Lin, S.-D. Jiang, J. Tang, B.-W. Wang, S. Gao, *Chem.-Eur. J.* **2011**, *17*, 12476-12481.

[90] F. Pointillart, K. Bernot, S. Golhen, B. Le Guennic, T. Guizouarn, L. Ouahab, O. Cador, *Angew. Chem. Int. Ed*. **2015**, *54*, 1504-1507.

[91] A. Abragam, B. Bleaney, Electron Paramagnetic Resonance of Transition Ions, Dover Publications, New York, 1986.

[92] N. Ishikawa, M. Sugita, W. Wernsdorfer, *J. Am. Chem. Soc.* **2005**, *127*, 3650 –3651.

[93] N. Ishikawa, M. Sugita, W. Wernsdorfer, *Angew. Chem. Int. Ed.* **2005**, *44*, 2931 – 2935; *Angew. Chem.* **2005**, *117*, 2991-2995.

[94] F. Tuna, C. A. Smith, M. Bodensteiner, L. Ungur, L. Chibotaru, E. J. L. McInnes, R. E. P. Winpenny, D. Collison, R. A. Layfield, *Angew. Chem. Int. Ed.* **2012**, *51*, 6976 – 6980; *Angew. Chem.* **2012**, *124*, 7082 – 7086.

[95] W. J. Childs, *Phys. Rev. A*, **1970**, 2, 169.

[96] J. F. Gonzalez, F. Pointillart, O. Cador, *Inorg. Chem. Front.* **2019**, *6*, 1081-1086.

[97] K. Katoh, K. Umetsu, B. K. Breedlove, M. Yamashita, *Sci. China Chem.* **2012**, *55*, 918- 925.

[98] M. Waters, F. Moro, I. Krivokapic, J. Mcmaster, J. van Slageren, *Dalton Trans.* **2012**, *41*, 1128-1130.

[99] L. Tesi, Z. Salman, I. Cimatti, F. Pointillart, K. Bernot, M. Mannini, R. Sessoli, *Chem. Commun.* **2018**, *54*, 7826-7829.

[100] J. Ferrando-Soria, E. M. Pineda, A. Chiesa, A. Fernandez, S. A. Magee, S. Carretta, P. Santini, I. J. Vitorica-Yrezabal, F. Tuna, G. A. Timco, E. J. L. McInnes, R. E. P. Winpenny, *Nat. Commun*. **2016**, *7*, 11377.

[101] C. Godfrin, A. Ferhat, R. Ballou, S. Klyatskaya, M. Ruben, W. Wernsdorfer, F. Balestro, *Phys. Rev. Lett.* **2017**, *119*, 187702.

[101] M. Atzori, A. Chiesa, E. Morra, M. Chiesa, L. Sorace, S. Carretta, R. Sessoli, *Chem. Sci.* **2018**, *9*, 6183-6192.

[102] N. A. Spaldin, M. Fiebig, *Science* **2005**, *309*, 391–392.

[103] W. Eerenstein,N. D. Mathur, J. F. Scott, *Nature* **2006**, 442, 759–765.

[104] C. Train, R. Gheorghe, V. Krstic, L.-M. Chamoreau, N. S. Ovanesyan, G. L. J. A. Rikken, M. Gruselle, M. Verdaguer, *Nat. Mater.* **2008**, 7,729–734.

[105] L. Ouahab, T. Enoki, *Eur. J. Inorg. Chem.* **2004**, 933–941.

[106] F. Pointillart, Y. Le Gal, S. Golhen, O. Cador, L. Ouahab, *Chem. Commun.* **2009**, 3777–3779.

[107] F. Pointillart, B. Le Guennic, S. Golhen, O. Cador, L. Ouahab, *Chem. Commun.* **2013**, *49*, 11632–11634.

[108] H.-Y. Wang, J.-Y.; Ge, C. Hua, C.-Q. Jiao, Y. Wu, C. F. Leong, D. M. D'Alessandro, T. Liu, J.-L. Zuo, *Angewandte Chemie Int. Ed.* **2017**, 56, 5465–5470.

[109] J. Su, T.-H. Hu, R. Murase, H.-Y. Wang, D. M. D'Alessandro, M. Kurmoo, J.-L. Zuo, *Inorg. Chem.* **2019**, 58, 3698–3706.

[110] G. Fernandez Garcia, V. Montigaud, L. Norel, O. Cador, B. Le Guennic, F. Totti, F. Pointillart, *Magnetochemistry* **2019**, *5*, 46-59.

[111] N. Ishikawa, M. Sugita, N. Tanaka, T. Ishikawa, S.-Y. Koshihara, Y. Kaizu, *Inorg. Chem.* **2004**, *43*, 5498–5500.

[112] J. D. Rinehart, M. Fang, W. J. Evans, J. R. Long, J. R., *Nat. Chem.* **2011**, *3*, 538−542.

[113] J. D. Rinehart, M. Fang, W. J. Evans, J. R. Long, *J. Am. Chem. Soc.* **2011**, *133*, 14236−14239;

[114] S. Demir, M. Nippe, M. I. Gonzalez, J. R. Long, *Chem. Sci.* **2014**, *5*, 4701–4711.

[115] S. Demir, J. M. Zadrozny, M. Nippe, J. R. Long, *J. Am. Chem. Soc.* 2012, 134, 18546–18549.

[116] S. Demir, I.-R. Jeon, J. R. Long, T. D. Harris, *Coord. Chem. Rev.* **2015**, 289-290, 149-176.

[117] C. A. Gould, L. E. Darago, M. I. Gonzalez, S. Demir, J. R. Long, *Angew. Chem. Int. Ed.* **2017**, *56*, 10103-10107.

[118] J. Nakazaki, M. M. Matsushita, A. Izuoka, T. Sugawara, *Tetrahedron Lett.* **1999**, 40, 5027-5030.

[119] R. Kumai, M. M. Matsushita, A. Izuoka, T. Sugawara, *J. Am. Chem. Soc.* **1994**, *116*, 4523-4524.

[120] H. Komatsu, R. Mogi, M. M. Matsushita, T. Miyagi, Y. Kawada, T. Sugawara, *Polyhedron* **2009**, *28*, 996-2000.

[121] H. Komatsu, M. M. Matsushita, S. Yamamura, Y. Sugawara, K. Susuki, T. Sugawara, *J. Am. Chem. Soc.* **2010**, *132*, 4528-4529.

[122] S. Venneri, J. M. Wilson J. Rawson, M. Pilkington, *ChemPlusChem* **2015**, *80*, 1624-1633.

[123] J. Guasch, L. Grisanti, V. Lloveras, J. Vidal-Gancedo, M. C. Souto, D. Morales, M. Vilaseca, C. Sissa, A. Painelli, I. Ratera, C. Rovira, J. Veciana, *Angew. Chem. Int. Ed.* **2012**, *51*, 11024-11028.

[124] J. Guash, L. Grisanti, M. Souto, V. Lloveras, J. Vidal-Gancedo, I. Ratera, A. Painelli, C. Rovira, J. Veciana, *J. Am. Chem. Soc.* **2013**, *135*, 6958-6967.

[125] M. Souto, J. Guasch, V. Lloveras, P. T. Mayorga, J. Lopez Navarrete, J. Casado, I. Ratera, C. Rovira, A. Painelli, J. Veciana, *J. Phys. Chem. Lett.* **2013**, *4*, 2721-2726.

[126] M. Souto, D. Morales, J. Guasch, I. Ratera, C. Rovira, A. Painelli, J. Veciana, *J. Phys. Org. Chem.* **2014**, *27*, 465-469.

[127] M. Souto, M. Solano, M. Jensen, D. Bendixen, F. Delchiaro, A. Girlando, A. Painelli, J. O. Jeppesen, C. Rovira, I. Ratera, J. Veciana, *Chem. Eur. J.* **2015**, *21*, 8816-8825.

[128] S. Shimono, R. Tamura, N. Ikuma, T. Takimoto, N. Kawame, O. Tamada, N. Sakai, H. Matsuura, J. Yamauchi, *J. Org. Chem.* **2004**, *69*, 475-481.

[129] A. Rajca, M. Pink, S. Mukherjee, S. Rajca, K. Das, *Tetrahedron* **2007**, *63*, 10731-10742.

[130] V. K. Praveen, Y. Yamamoto, T. Fukushima, Y. Tsunobuchi, K. Nakabayashi, S.-I. Ohkoshi, K. Kato, M. Takata, T. Aida, *Chem. Commun.* **2015**, *51*, 1206-1209.

[131] H. Douib, M. Puget, Y. Suffren, F. Pointillart, K. Bernot, B. Le Guennic, O. Cador, A. Gouasmia, L. Ouahab, *Dyes and Pigments* **2017**, *145*, 285-293.

[132] J. H. Osiecki, E. F. Ullman, *J. Am. Chem. Soc.* **1968**, *90*, 1078-1079.

[133] M. Feng, F. Pointillart, B. Le Guennic, B. Lefeuvre, S. Golhen, O. Cador, O. Maury, L. Ouahab, *Chem. Asian J.* **2014**, *9*, 2814-2825.

[134] K. Kodama, A. Kobayashi, T. Hirose, *Tetrahedron Lett.*, **2013**, *54*, 5514–5517.

[135] S. Speed, M. Feng, G. Fernandez Garcia, F. Pointillart, B. Lefeuvre, F. Riobé, S. Golhen, B. Le Guennic, F. Totti, Y. Guyot, O. Cador, O. Maury, L. Ouahab, *Inorg. Chem. Front.* **2017**, *4*, 604-617.

[136] C. Dekker, A. F. M. Arts, H. W. Wijn, A. J. van Duyneveldt, J. A. Mydosh, *Phys. Rev. B: Condens. Matter,* **1989**, *40*, 11243.

[137] K. S. Cole, R. H. Cole, *J. Chem. Phys*. **1941**, *9*, 341-351.

[138] K. E. Henegar, S. W. Ashford, T. A. Baughman, J. C. Sih, R.-L. Gu, *J. Org. Chem.* **1997**, *62*, 6588-6597.

[139] C. M. Elhaïk Pask, C. A. Kilner, M. A. Halcrow, *Tetrahedron* **2007**, *63*, 291-298.

[140] A. Paul, A. P. C. Ribeiro, A. Karmakar, M. Fatima, C. Guedes da Silva, A. J. L. Pombeiro, *Dalton Trans.* **2016**, *45*, 12779-12789.

[141] M. Feng, F. Pointillart, B. Lefeuvre, V. Dorcet, S. Golhen, O. Cador, L. Ouahab, *Inorg. Chem.* **2015**, *54*, 4021-4028.

[142] O. Galangau, V. Montigaud, J. Flores Gonzalez, B. lefeuvre, V. Dorcet, B. Le Guennic, O. Cador, L . Ouahab, F. Pointillart*, Polyhedron* **2019**, *168*, 28-36.

[143] R. J. Blagg, L. Ungur, F. Tuna, J. Speak, P. Comar, D. Collinson, W. Wernsdorfer, E. J. L. McInnes, L. F. Chibotaru, R. E. P. Winpenny, *Nat. Chem.* **2013**, *5*, 673−678.

[144] J. Ruiz, A. J. Mota, A. Rodriguez-Diguez, S. Titos, J.-M. Herrera, E. Ruiz, E. Cremades, J.-P. Costes, E. Colacio, *Chem. Commun.* **2012**, *48*, 7916−7918.

[145] Y.-N. Guo, G.-F. Xu, W. Wernsdorfer, Y. Guo, H.-J. Zhang, *J. Am. Chem. Soc.* **2011**, *133*, 11948−11951.

[146] A. Venugopal, F. Tuna, T. R. Spaniol, L. Ungur, L. F. Chibotaru, J. Okuda, R. A. Layfield, *Chem. Commun.* **2013**, *49*, 901−903.

[147] Y.-N. Guo, G.-F. Xu, Y. Guo, J. Tang, *Dalton Trans.* **2011**, *40*, 9953−9963.

[148] X. Yi, K. Bernot, V. Le Corre, G. Calvez, F. Pointillart, O. Cador, B. Le Guennic, J. Jung, O. Maury, V. Placide, Y. Guyot, T. Roisnel, C. Daiguebonne, O. Guillou, *Chem. Eur. J.* **2014**, *20*, 1569-1576.

[149] F. Pointillart, Y. Le Gal, S. Golhen, O. Cador, L. Ouahab, *Chem. Eur. J.* **2011**, *17*, 10397-10404.

[150] R. Sessoli, A. K. Powell, *Coord. Chem. Rev.* **2009**, *253*, 2328-2341.

[151] P. H. Lin, T. J. Burchell, L. Ungur, L. F. Chibotaru, W. Wernsdorfer, M. Murugesu, *Angew. Chem.* **2009**, *121*, 9653 –9656; *Angew. Chem. Int. Ed.* **2009**, *48*, 9489 – 9492.

[152] Y.-N. Guo, G.-F. Xu, W. Wernsdorfer, L. Ungur, Y. Guo, J. Tang, H.- J. Zhang, L. F. Chibotaru, A. K. Powell, *J. Am. Chem. Soc.* **2011**, *133*, 11948 – 11951.

[153] J. Long, F. Habib, P. H. Lin, I. Korobkov, G. Enright, L. Ungur, W. Wernsdorfer, L. F. Chibotaru, M. Murugesu, *J. Am. Chem. Soc.* **2011**, *133*, 5319 –5328.

[154] R. A. Layfield, J. J. W. McDouall, S. A. Sulway, F. Tuna, D. Collison, R. E. P. Winpenny, *Chem. Eur. J.* **2010**, *16*, 4442 –4446.

[155] K. Katoh, T. Kajiwara, M. Nakano, Y. Nakazawa, W. Wernsdorfer, N. Ishikawa, B. K. Breedlove, M. Yamashita, *Chem. Eur. J.* **2011**, *17*, 117 – 122.

[156] G. F. Xu, Q. L. Wang, P. Gamez, Y. Ma, R. Clerac, J. K. Tang, S. P. Yan, P. Cheng, D. Z. Liao, *Chem. Commun.* **2010**, *46*, 1506 –1508.

[157] W. Wernsdorfer, N. Aliaga-Alcalde, D. Hendrickson, G. Christou, *Nature* **2002**, *416*, 406-409.

[158] F. Pointillart, T. Guizouarn, B. Lefeuvre, S. Golhen, O. Cador, L. Ouahab, *Chem. Eur. J.* **2015**, *21*, 16929-16934.

[159] J.-K. Ou-Yang, N. Saleh, G. Fernandez-Garcia, L. Norel, F. Pointillart, T. Guizouarn, O. Cador, F. Totti, L. Ouahab, J. Crassous, B. Le Guennic, *Chem. Commun.* **2016**, *52*, 14474-14477.

[160] Y. Shen, C.-F. Chen, Helicenes Chemistry: From Synthesis to Applications; Springer: Berlin, 2017.

[161] T. Biet, A. Fihey, T. Cauchy, N. Vanthuyne, C. Roussel, J. Crassous, N. Avarvari, *Chem. Eur. J.* **2013**, *19*, 13160-13167.

[162] F. Pointillart, J.-K. Ou-Yang, G. Fernandez-Garcia, V. Montigaud, J. Flores Gonzalez, R. Marchal, L. Favereau, F. Totti, J. Crassous, O. Cador, L. Ouahab, B. Le Guennic, *Inorg. Chem.* **2019**, *58*, 52-56.

[163] F. Gao, X.-M. Zhang, L. Cui, K. Deng, Q.-D. Zeng, J.-L. Zuo, *Sci. Reports*, **2014**, *4*, 5928-5964.

A library of TTF-based ligands was elaborated from a common molecular skeleton by its alkylation by chelating, paramagnetic and chiral arms. Using such library of ligands, lanthanide complexes were designed allowing to understand the effect of supramolecular interaction, electronic distribution and hyperfine coupling on the SMM behavior. Multi-SMM behavior as well as auto-assembly of SMM were rationally obtained.

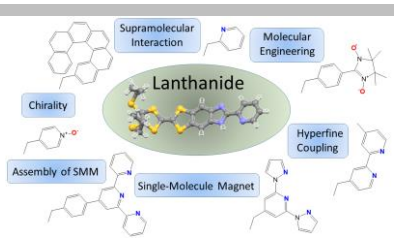

TTF lanthanide complexes

*Olivier Cador, Boris le Guennic, Lahcène Ouahab, Fabrice Pointillart,**

Page No. – Page No.

Decorated Tetrathiafulvalene-Based Ligands: Powerful Chemical Tools for the Design of Single-Molecule Magnets